

UNIVERSIDAD SAN FRANCISCO DE QUITO USFQ

Colegio de Ciencias e Ingeniería

**Processing of data measurements of  
radiation fields at flight altitudes with  
the pixel detector Timepix**

**María del Carmen Salazar Reinoso**

**Física**

Trabajo de titulación presentado como requisito  
para la obtención del título de

Física

Quito, 18 de agosto de 2003

**UNIVERSIDAD SAN FRANCISCO DE QUITO USFQ**

**Colegio de Ciencias e Ingeniería**

**HOJA DE CALIFICACIÓN DE TRABAJO DE FIN DE  
CARRERA**

**María del Carmen Salazar Reinoso**

Nombre del profesor, Título académico: Edgar Carrera, PhD

Nombre del profesor, Título académico: Hab. prof. Carlos Granja, PhD

Quito, 18 de agosto de 2003

## © Derechos de Autor

Por medio del presente documento certifico que he leído todas las Políticas y Manuales de la Universidad San Francisco de Quito USFQ, incluyendo la Política de Propiedad Intelectual USFQ, y estoy de acuerdo con su contenido, por lo que los derechos de propiedad intelectual del presente trabajo quedan sujetos a lo dispuesto en esas Políticas.

Asimismo, autorizo a la USFQ para que realice la digitalización y publicación de este trabajo en el repositorio virtual, de conformidad a lo dispuesto en la Ley Orgánica de Educación Superior del Ecuador.

Nombres y apellidos: María del Carmen Salazar Reinoso

Código: 00207086

Cédula de Identidad: 1718594227

Lugar y fecha: Quito, 18 de agosto de 2003

## ACLARACIÓN PARA LA PUBLICACIÓN

**Nota:** El presente trabajo, en su totalidad o cualquiera de sus partes, no debe ser considerado como una publicación, incluso a pesar de estar disponible sin restricciones a través de un repositorio institucional. Esta declaración se alinea con las prácticas y recomendaciones presentadas por el Committee on Publication Ethics COPE descritas por Barbour et al. (2017) Discussion document on best practice for issues around theses publishing, disponible en <http://bit.ly/COPETheses>

## UNPUBLISHED DOCUMENT

**Note:** The following capstone project is available through Universidad San Francisco de Quito USFQ institutional repository. Nonetheless, this project – in whole or in part – should not be considered a publication. This statement follows the recommendations presented by the Committee on Publication Ethics COPE described by Barbour et al. (2017) Discussion document on best practice for issues around theses publishing available on <http://bit.ly/COPETheses>

# Agradecimientos

A mis padres, Carlos y Carmen, por su apoyo y guía en cada decisión a lo largo de este camino. A mi hermana, por ser incondicional y animarme en momentos de incertidumbre. A mis amigos: Mateo, Alejo y Vale, por hacer de este trayecto algo inolvidable que recordaré con mucho cariño. Al Jose, por nunca soltar mi mano y acompañarme en cada paso a lo largo de estos años. A mis abuelos, por siempre velar por mí. A Edgar Carrera, por sus oportunos comentarios y observaciones, que permitieron entregar la mejor versión de este trabajo. Finalmente, quiero expresar un agradecimiento especial a Carlos Granja ya que este proyecto no habría sido posible sin su mentoría, paciencia y apoyo.

# Resumen

En este trabajo se procesaron datos experimentales del campo de radiación mixta en el interior de aviones de pasajeros en la atmósfera a altitudes aéreas (10-12 km). Los datos detallados fueron medidos por el detector de píxeles semiconductor Timepix operado en una cámara de radiación miniaturizada MiniPIX-Timepix, el cual proporciona caracterización precisa, sensibilidad cuántica en términos de energía depositada y la visualización de radiación de partículas cargadas. Los datos se procesaron con una herramienta SW integrada (Data Processing Engine-DPE). Los resultados y productos de parámetros físicos consisten en flujo de partículas, tasa de dosis, energía depositada, dosis depositada, composición del campo en amplias clases de partículas (protones, electrones, rayos X), así como la visualización detallada del campo de radiación y registro de imágenes cuánticas de huellas de partículas individuales. En la parte principal de este trabajo se presenta el análisis detallado de dos mediciones, así como gráficos comparativos de resultados seleccionados entre todos los vuelos. Los resultados de la dosis total absorbida se comparan con los valores medidos en tierra y en órbita LEO a bordo de un satélite. Junto con una interpretación física completa, los resultados obtenidos serán el contenido de un futuro artículo de investigación en una revista científica.

Palabras clave: *detección de radiación, radiación en la atmósfera, detectores de pixeles, física nuclear, física de partículas, rayos cósmicos*

# Abstract

In this thesis, experimental data of the mixed-radiation field inside passenger aircraft in the atmosphere at airline altitudes (10-12 km) were processed. High-resolution data were measured by the semiconductor pixel detector Timepix operated in a miniaturized radiation camera MiniPIX-Timepix. The detector provides precise characterization, quantum sensitivity in terms of deposited energy and visualization of the charged particle radiation and X-ray field. The data were processed at the pre-processing and processing level with an integrated SW tool (Data Processing Engine-DPE). Results and physics data products consist of particle flux, dose rate, deposited energy, deposited dose, field composition into broad particle classes (protons, electrons, X rays) as well as detailed visualization of the radiation field and quantum imaging registration of single particle tracks. In the main part of this work the detailed analysis of two measurements, as well as comparative graphs of selected results between all flights is presented. Results of total absorbed dose are compared with values measured on ground and in LEO orbit onboard a satellite. Together with a complete physics interpretation, the results obtained will be considered for a future research article at a scientific journal.



Keywords: *radiation detection, radiation in the atmosphere, particle tracking, radiation imaging, pixel detectors, nuclear physics, particle physics, cosmic rays*

# Contents

<b>1</b>	<b>Introduction</b>	<b>20</b>
1.1	Ionizing Radiation . . . . .	21
1.2	Radiation in the atmosphere . . . . .	24
1.3	Semiconductor pixel detector Timepix . . . . .	25
<b>2</b>	<b>Methodology</b>	<b>27</b>
2.1	Radiation Camera MiniPIX-Timepix . . . . .	27
2.2	Quantum-imaging detection of radiation . . . . .	29
2.3	Measurements . . . . .	31
2.4	Raw Data . . . . .	33
2.5	Data Processing . . . . .	34

	10
2.5.1 Pre-Processing . . . . .	35
2.5.2 Processing . . . . .	36
2.5.3 Post-Processing . . . . .	38
<b>3 Results</b>	<b>40</b>
3.1 Detection and visualization of radiation field . . . . .	41
3.2 Composition characterization . . . . .	43
3.3 Event count rates . . . . .	46
3.4 Particle fluxes . . . . .	48
3.4.1 Selected flights . . . . .	49
3.4.2 All flights . . . . .	50
3.5 Deposited Energy . . . . .	52
3.5.1 Time distribution . . . . .	52
3.5.2 Deposited Energy Spectra . . . . .	56
3.6 Dose rates . . . . .	57
3.6.1 Selected flights . . . . .	57

	11
3.6.2 All flights . . . . .	59
3.7 Dose . . . . .	60
3.8 Linear-energy-transfer spectra . . . . .	62
<b>4 Conclusions</b>	<b>63</b>
<b>5 Annexes</b>	<b>66</b>
5.1 Particle fluxes for remaining measurements . . . . .	66
5.1.1 Total particle flux, all particles . . . . .	66
5.1.2 Particle flux, according to particle class . . . . .	71
5.2 Deposited energy for remaining measurements . . . . .	76
5.2.1 Deposited energy, all particles . . . . .	76
5.2.2 Deposited energy according to particle class . . . . .	80
5.3 Dose rate for remaining measurements . . . . .	85
5.3.1 Total dose rate, all particles . . . . .	85
5.3.2 Dose rate according to particle class . . . . .	89
<b>References</b>	<b>93</b>

# List of Tables

2.1	List of data of flights evaluated in this work. . . . .	32
3.1	Classes/Filters for tracks . . . . .	44
3.2	Number and percentage of each particle class detected on flights <b>B</b> and <b>G</b> from the Sampling list obtained in the post-processing stage.	47
3.3	Total particle count, measured live time and flux for each measurement	48
3.4	Particle flux by class of flights <b>B</b> and <b>G</b> obtained from the Sampling list in the post-processing stage. . . . .	50
3.5	Deposited energy average in keV by particle class during the sam- pling time in minutes for measurements <b>B</b> and <b>G</b> described in Table 2.1. . . . .	54
3.6	Dose rate, total dose and standard deviation during each flight, described in Table 2.1. . . . .	60

# List of Figures

1.1	Charged energetic particles detected with a MiniPIX-Timepix 300 $\mu\text{m}$ detector . . . . .	23
1.2	Illustration explaining the origin of secondary cosmic rays . . . . .	25
1.3	Photo (a) and illustration (b) of the Timepix chip assembly . . . . .	26
2.1	Miniaturized radiation camera MiniPIX Timepix. . . . .	28
2.2	Example of radiation measured by Timepix 300 $\mu\text{m}$ Si sensor during flight <b>B</b> described in Table 2.1. . . . .	30
2.3	Quantum imaging detection and pixel-scale spectrometry of single particles (alpha particles, low-energy gamma rays, X rays) . . . . .	30
2.4	Illustration of the detector operation. . . . .	32
2.5	Illustration of the two possible geometries for positioning the detector with respect to the earth's horizon line. . . . .	33

2.6	Example of raw data file. The data is collected in consecutive frames, with an acquisition time of 10 seconds, during which time single particles are registered. . . . .	34
2.7	Elist data file of processed single particles (listed in rows) each with detailed imaging, spectral and tracking values (listed in columns) of measurement <b>B</b> described in Table 2.1. . . . .	37
2.8	Sampling list file of measurement <b>B</b> described in Table 2.1. The sampling list file evaluates the physical quantities of the radiation field measured (particle fluxes, dose rates, deposited dose) in fixed time intervals e.g., 1 min. . . . .	38
3.1	Detection and track visualization of the mixed-radiation field produced during the short flight <b>B</b> . . . . .	41
3.2	Detection and track visualization of the mixed-radiation field produced during the long flight <b>G</b> at the beginning and at the end of the flight. . . . .	42
3.3	Plot of integrated tracks of selected particles for short flight <b>B</b> . . .	44
3.4	Plot of integrated tracks of selected particles for long flight <b>G</b> . . . .	45
3.5	Particle event count rates for the whole measurement for short flight <b>B</b> . . . . .	46

	15
3.6 Particle event count rates for the whole measurement for long flight <b>G</b> . . . . .	46
3.7 Flux for the whole measurement for short flight <b>B</b> . . . . .	49
3.8 Flux for the whole measurement for long flight <b>G</b> . . . . .	49
3.9 Flux for the whole measurement for all short and long flights described in Table 2.1. . . . .	51
3.10 Photons and electrons flux for the whole measurement for all short and long flights described in Table 2.1. . . . .	51
3.11 Deposited energy for the whole measurement for short flight <b>B</b> . . .	53
3.12 Deposited energy for the whole measurement for long flight <b>G</b> . . . .	53
3.13 Total deposited energy for the whole measurement for all short and long flights described in Table 2.1, measured in keV per minute. . .	54
3.14 Deposited energy of protons for the whole measurement for all short and long flights described in Table 2.1. . . . .	55
3.15 Deposited energy of photons and electrons for the whole measurement for all short and long flights described in Table 2.1. . . . .	55
3.16 Deposited energy spectra of flights <b>B</b> and <b>G</b> described in Table 2.1.	56
3.17 Dose rate for whole measurement for short flight <b>B</b> . . . . .	58



	16
3.18 Dose rate for whole measurement for long flight <b>G</b> . . . . .	58
3.19 Dose rate for the whole measurement for (a) short and (b) long flight described in Table 2.1. . . . .	59
3.20 Average dose rate and total dose of all flights during the whole measurement time, which was different for each flight. . . . .	61
3.21 Linear energy transfer distributions . . . . .	62
5.1 Total particle flux for the whole measurement <b>A</b> . . . . .	66
5.2 Total particle flux for the whole measurement <b>C</b> . . . . .	67
5.3 Total particle flux for the whole measurement <b>D</b> . . . . .	67
5.4 Total particle flux for the whole measurement <b>E</b> . . . . .	68
5.5 Total particle flux for the whole measurement <b>F</b> . . . . .	68
5.6 Total particle flux for the whole measurement <b>H</b> . . . . .	69
5.7 Total particle flux for the whole measurement <b>I</b> . . . . .	69
5.8 Total particle flux for the whole measurement <b>J</b> . . . . .	70
5.9 Particle flux for the whole measurement <b>A</b> . . . . .	71
5.10 Particle flux for the whole measurement <b>C</b> . . . . .	72

	17
5.11 Particle flux for the whole measurement <b>D</b> . . . . .	72
5.12 Particle flux for the whole measurement <b>E</b> . . . . .	73
5.13 Particle flux for the whole measurement <b>F</b> . . . . .	73
5.14 Particle flux for the whole measurement <b>H</b> . . . . .	74
5.15 Particle flux for the whole measurement <b>I</b> . . . . .	74
5.16 Particle flux for the whole measurement <b>J</b> . . . . .	75
5.17 Deposited energy for the whole measurement <b>A</b> . . . . .	76
5.18 Deposited energy for the whole measurement <b>C</b> . . . . .	76
5.19 Deposited energy for the whole measurement <b>D</b> . . . . .	77
5.20 Deposited energy for the whole measurement <b>E</b> . . . . .	77
5.21 Deposited energy for the whole measurement <b>F</b> . . . . .	78
5.22 Deposited energy for the whole measurement <b>H</b> . . . . .	78
5.23 Deposited energy for the whole measurement <b>I</b> . . . . .	79
5.24 Deposited energy for the whole measurement <b>J</b> . . . . .	79
5.25 Deposited energy for the whole measurement <b>A</b> . . . . .	80
5.26 Deposited energy for the whole measurement <b>C</b> . . . . .	81

	18
5.27 Deposited energy for the whole measurement <b>D</b> . . . . .	81
5.28 Deposited energy for the whole measurement <b>E</b> . . . . .	82
5.29 Deposited energy for the whole measurement <b>F</b> . . . . .	82
5.30 Deposited energy for the whole measurement <b>H</b> . . . . .	83
5.31 Deposited energy for the whole measurement <b>I</b> . . . . .	83
5.32 Deposited energy for the whole measurement <b>J</b> . . . . .	84
5.33 Dose rate for the whole measurement <b>A</b> . . . . .	85
5.34 Dose rate for the whole measurement <b>C</b> . . . . .	85
5.35 Dose rate for the whole measurement <b>D</b> . . . . .	86
5.36 Dose rate for the whole measurement <b>E</b> . . . . .	86
5.37 Dose rate for the whole measurement <b>F</b> . . . . .	87
5.38 Dose rate for the whole measurement <b>H</b> . . . . .	87
5.39 Dose rate for the whole measurement <b>I</b> . . . . .	88
5.40 Dose rate for the whole measurement <b>J</b> . . . . .	88
5.41 Dose rate for the whole measurement <b>A</b> . . . . .	89
5.42 Dose rate for the whole measurement <b>C</b> . . . . .	90

	19
5.43 Dose rate for the whole measurement <b>D</b> . . . . .	90
5.44 Dose rate for the whole measurement <b>E</b> . . . . .	91
5.45 Dose rate for the whole measurement <b>F</b> . . . . .	91
5.46 Dose rate for the whole measurement <b>H</b> . . . . .	92
5.47 Dose rate for the whole measurement <b>I</b> . . . . .	92
5.48 Dose rate for the whole measurement <b>J</b> . . . . .	93

# Chapter 1

## Introduction

There are several reasons to study and measure the radiation field in aircrafts at flight altitudes[1]. Although we are all exposed to a certain dose of radiation in our daily lives, aircrew members and passengers are subjected to a higher radiation exposure rate than people on the ground under natural conditions [2].

The increase in ionising radiation with increasing altitude is due to the interaction of the galactic cosmic radiation (GCR) with the atoms of the atmosphere. The charge and energy spectra of primary particles are modified by energy loss and nuclear interactions, and various secondary particles are created as a result [2].

According to the ICRP (International Commission on Radiological Protection) recommendations [3], the exposure of aircrew members to cosmic radiation in jet aircraft should be regarded as occupational exposure, so monitoring the radiation

exposure of crew and passengers is not just important, but necessary. It also serves to study the effects of radiation on electronic and avionics components [4], as well as space weather physics in the atmosphere at airline altitudes[5].

These measurements play an important role for the detection and study of energetic and highly variable solar particle events (SPE) and coronal mass ejections[5].

## 1.1 Ionizing Radiation

Ionizing radiation is generally characterized by its ability to excite and ionize the atoms of matter with which it interacts. Since the energy required for a valence electron to escape from an atom is of the order of 4-25 eV, radiation must carry kinetic or quantum energies in excess of this magnitude to be called “ionizing” [6]. As is evident from equation 1.1, this criterion would appear to include electromagnetic radiation with wavelengths up to 320 nm, which includes most of the ultraviolet (UV) radiation band ( $\sim 10\text{-}400$  nm). However, these marginally ionizing UV radiation are less able to pass through matter than visible light, whereas other ionizing radiations are usually more penetrating [6].

$$E_{\gamma} = h\nu = \frac{hc}{\lambda} = \frac{1.2398 \text{ keV}}{\lambda} \quad (1.1)$$

In equation 1.1,  $\lambda$  is given in nm,  $h$  is the Planck’s constant  $h = 6.626 \times 10^{-34}$  J·s or  $4,136 \times 10^{-18}$  keV· s and  $c$  is the speed of light  $c = 2.998 \times 10^8$  m/s.

The important types of ionizing radiation to be considered are:

1.  **$\gamma$  rays:** Electromagnetic radiation of the shortest wave length and highest energy, resulting from the radioactive disintegration of atomic nuclei and formed by photons. Natural sources of gamma rays originating on Earth are mainly the result of radioactive decay and secondary radiation from atmospheric interactions with cosmic ray particles.
2. **X-rays:** Electromagnetic radiation emitted by charged particles (usually electrons) in changing atomic energy levels (called characteristic or fluorescence x-rays) or in slowing down in a Coulomb force field (continuous or bremsstrahlung x-rays) [6].
3. **Heavy Charged Particles (HCPs):** Usually obtained from the acceleration by a Coulomb force field in a Van de Graaff, cyclotron, or heavy-particle linear accelerator [6]. Heavy charged particles are all energetic ions with a mass of one atomic mass unit or greater, such as protons, alpha particles (helium nuclei), pions or fission fragments [7].
4. **Low Charged Particles (LCPs):** Include electrons; if positive in charge, they are called positrons. If they are emitted from a nucleus, they are usually referred to as  $\beta$ -rays (positive or negative). If they result from a charged particle collision, they are referred to as “ $\delta$ -rays” [6], [7].
5. **Neutrons:** Neutral particles obtained from nuclear reactions [e.g.,(p,n)or fission], since they cannot themselves be accelerated electrostatically [6].

Example of detection and track visualization of some charged energetic particles are shown in Figure 1.1

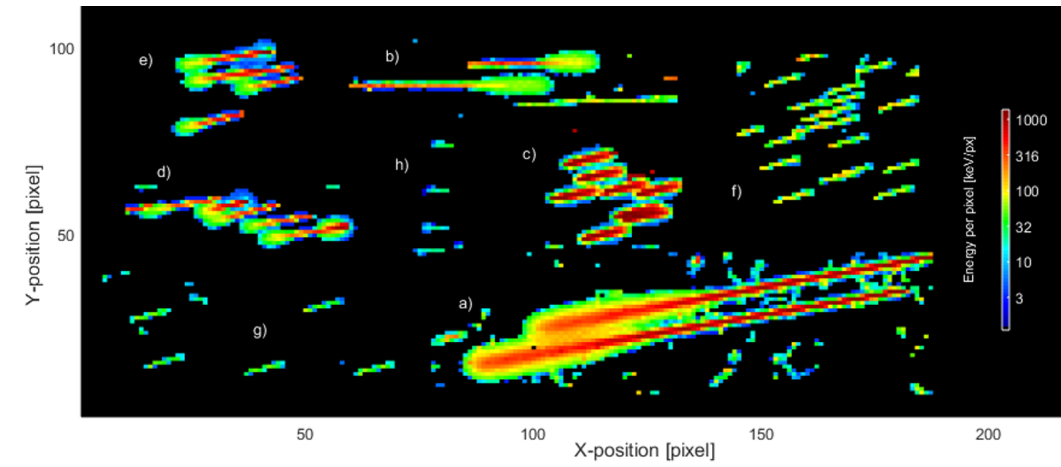


Figure 1.1: Charged energetic particles detected with a MiniPIX-Timepix  $300 \mu\text{m}$  detector (which will be described later) measured in particle accelerators. Ions (a-c). Protons (d-g) and electrons (h) in different directions and with different energies are displayed. Per-pixel energy response is shown by the color bar (in keV/px, log scale). About one third of the sensor matrix is shown ( $110 \times 215$  pixels =  $6 \text{ mm} \times 12 \text{ mm}$ ) [8].

The ICRU (International Commission on Radiation Units and Measurements) [9] has recommended certain terminology to refer to ionizing radiation that emphasizes the great differences between the interactions of charged and uncharged radiation with matter:

- **Directly Ionizing Radiation:** Fast charged particles, which deliver their energy to matter directly through many small Coulomb-force interactions along the particle's track.
- **Indirectly Ionizing Radiation:** Includes X or  $\gamma$  rays, photons or neutrons, which first transfer their energy to charged particles in the matter through which they pass in a relatively few large interactions.



## 1.2 Radiation in the atmosphere

Cosmic rays, which can originate from the sun, our own galaxy or other astrophysical systems, are high-energy particles that move through space. They may enter the Earth's atmosphere at some point along their course. The majority of cosmic rays are made up of protons and heavier atomic nuclei [10]. When one of the primary incident rays interacts with the components of the Earth's atmosphere, the charge and energy spectra of these initial particles are modified, thus a succession of derived particle rays, called secondary, are produced as seen in Figure 1.2. Some of these particles reach the surface while most of them are deflected off into space by the magnetosphere or heliosphere.

It makes sense, then, that at higher altitude there is higher ionising radiation. The radiation field contains variable contributions of hadrons, muons, and electron-photon constituents, depending on altitude as a measure of the amount of matter passed. The flux of primary GCR particles at the top of the atmosphere determines the number of secondary particles at a given position [11].

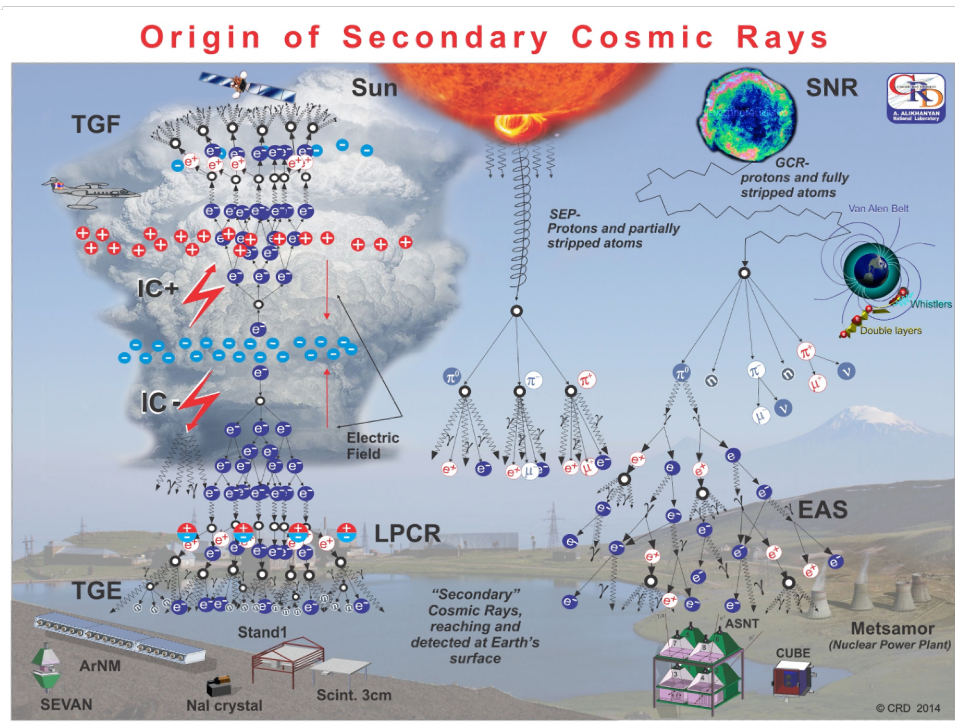


Figure 1.2: Illustration explaining how secondary cosmic rays are created [12].

### 1.3 Semiconductor pixel detector Timepix

The hybrid semiconductor pixel detector Timepix provides single-quantum sensitivity (photon counting), per-pixel spectrometry, high granularity, noiseless (dark-current free) detection and particle tracking capability [13]. The detector consists of a radiation sensitive semiconductor sensor, which is bump bonded to the pixelated readout ASIC Timepix chip as can be seen in Figure 1.3. It is equipped with highly integrated signal per-pixel (px) electronics (amplifier, amplitude discriminators, digital counter)[14].

These detectors can use sensors made of different material (Si,CdTe,GaAs) and thickness ( $100\ \mu\text{m}$ ,  $300\ \mu\text{m}$  and  $500\ \mu\text{m}$  for Si). The Timepix detector provides a highly density matrix of  $256 \times 256$  energy-sensitive pixels (total of 65.536 pixels) with pixel pitch of  $55\ \mu\text{m}$  and full area of  $14\ \text{mm} \times 14\ \text{mm} = 1.98\ \text{cm}^2$ [15]. The Timepix detector was configured to run in *counting operating* mode, which means 1-count for each signal over threshold (the counter is incremented by one when the energy of the interacting particle crosses the preset threshold level). The detector can be operated at room temperature without need for active cooling [15].

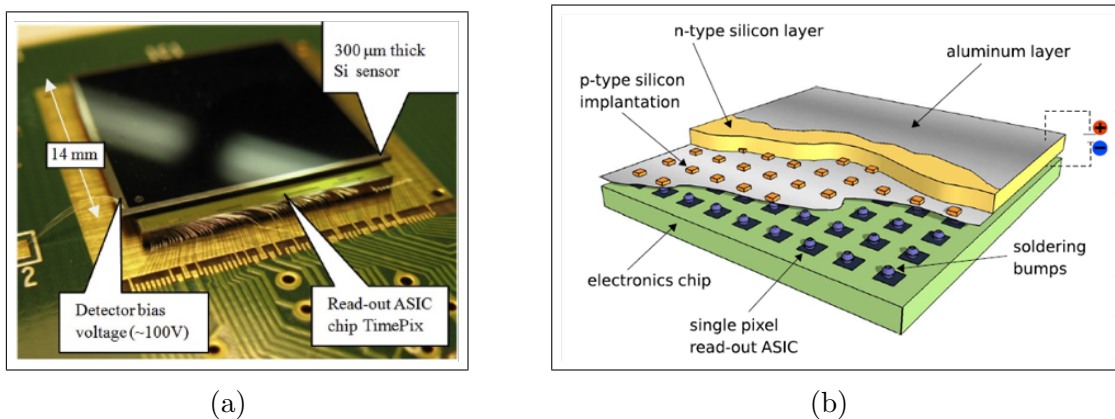


Figure 1.3: Photo (a) and illustration (b) of the Timepix chip assembly consisting of a semiconductor radiation sensitive sensor ( $300\ \mu\text{m}$  Silicon, full size  $14\text{mm} \times 14\text{mm}$ ) bump bonded to the ASIC Timepix readout chip [14].

# Chapter 2

## Methodology

The work presented is based on the high-sensitivity detection and precise measurement of radiation in low-intensity fields such as radiation in the atmosphere, space weather and cosmic rays. The measurements were performed with the radiation camera MiniPIX-Timepix, described in Sec. 2.1, in the passenger area of commercial aircrafts at several routes, as can be seen in Sec. 2.3.

### 2.1 Radiation Camera MiniPIX-Timepix

The pixel detector was used in the form of a compact radiation camera MiniPIX-Timepix. The MiniPIX is a miniaturized, low power consumption, single particle counting (or particle tracking) radiation camera (shown in Figure. 2.1) equipped with the semiconductor pixel detector Timepix. The standard MiniPIX system

incorporates single Timepix detector (256 x 256 pixels with pitch of 55  $\mu\text{m}$ ) with sensor according to customer preference, standardly 300  $\mu\text{m}$  thick silicon as it was used for this project. The chip-sensor array provides quantum imaging sensitivity for high-resolution spectral tracking of single particles in mixed radiation fields [8]. MiniPIX uses USB 2.0 interface capable to read up to 45 frames per second (with exposure time of 1 ms), weights 25 g, has a power of consumption of 1W and can be operated at room temperature without need for active cooling [16]. It is compatible with all major operating systems (MS Windows, Mac OS and LINUX). The software used to operate the detector, including online response, data readout and pre-processing is the PIXET software, which is supplied for free and can be run on a standard PC.

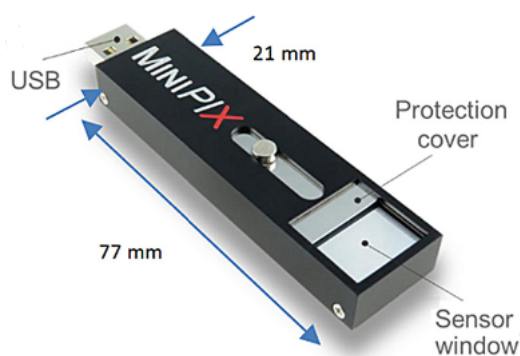


Figure 2.1: Miniaturized radiation camera MiniPIX Timepix. This camera has dimensions 77 mm  $\times$  21 mm  $\times$  10 mm and connects directly to PC or laptop via USB port [17].

## 2.2 Quantum-imaging detection of radiation

The hybrid architecture of Timepix detector provides fast and noiseless (dark-current free) detection of single quanta. It is energy sensitive in terms of deposited energy of low energy charged particles and X rays. The range of energies that it can detect goes from a few keV (X rays), tens of keV (electrons), hundreds of keV (protons) and few MeV (ions) [15]. For Silicon sensors a few tens of keV is the upper range for X rays and gamma rays. For charged particles it is essentially unlimited, including minimum-ionizing-particles.

An example of measured data is given in Figure 2.2, showing the detection and visualization of the radiation field in flight. The single particle tracks are displayed in *quantum-imaging* so-called counting mode at the pixel (px) level. All events are registered and processed. The color bar serves as an indicator of detected radiation (black= zero radiation detected, white= radiation detected). Low-energy transfer particles or LCPs such as x-rays and electrons produce small and narrow tracks. High-energy transfer particles or HCPs produce large and broad tracks [5].

An example of quantum imaging detection and per-pixel scale spectrometry of single particles is shown in Figure 2.3. Just a small region of the detector matrix is shown for detail and clarity. The data was taken from an  $^{241}\text{Am}$  radionuclide source of LE gamma rays identified by small signals of several pixels, X rays given by signals of 1 or 2 pixels and alpha particles given by large signals of many pixels [18].

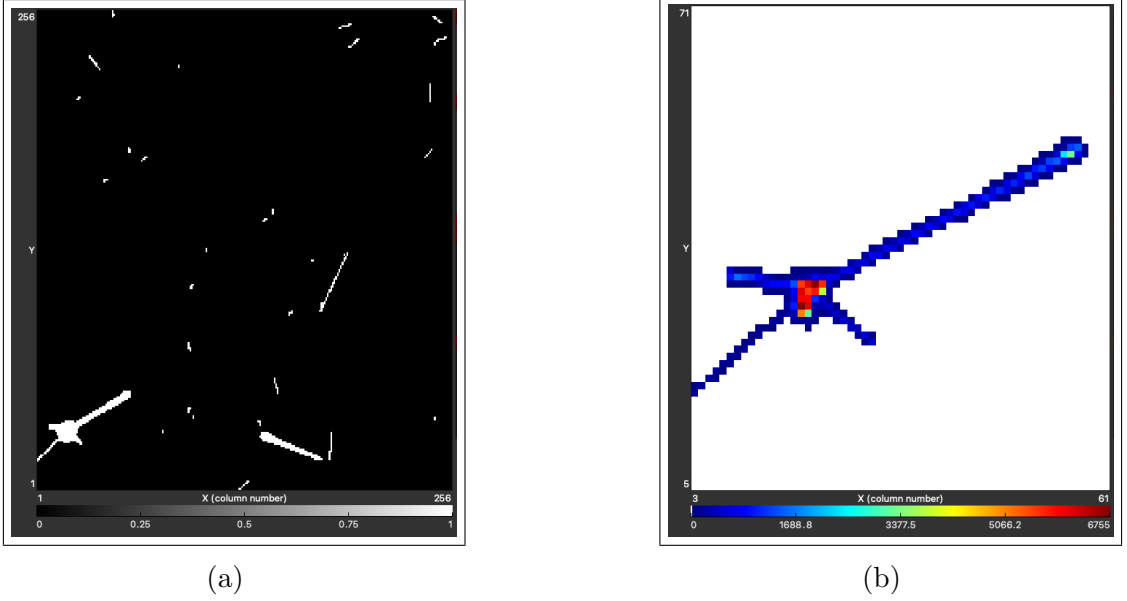


Figure 2.2: Example of radiation measured by Timepix 300  $\mu\text{m}$  Si sensor during flight **B** described in Table 2.1. In (a), the visualization of the radiation field observed during a 10-second interval in mid-flight at an altitude of 10 km can be seen. The entire sensor pixel matrix is shown (256 x 256 pixels = 1.98  $\text{cm}^2$ ). In (b), the detailed detection and visualization of a high LET event is shown. The per-px energy registration is displayed by the color scale in [keV/px]. Only a small region of the detector pixel matrix is displayed (58 x 66 pixels = 0.11  $\text{cm}^2$ ).

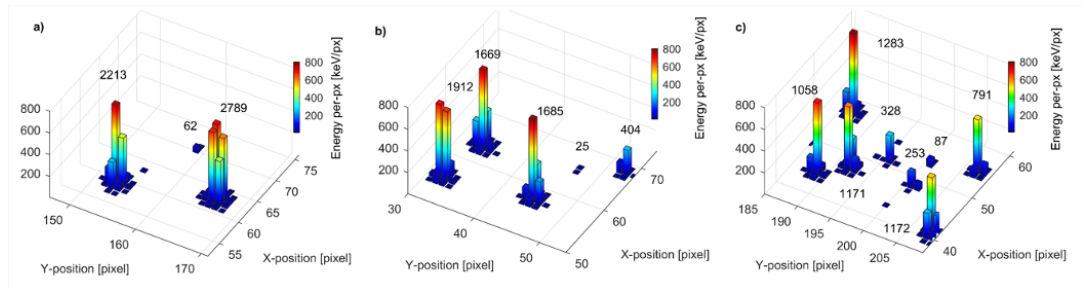


Figure 2.3: Quantum imaging detection and pixel-scale spectrometry (energy loss) of single particles (alpha particles, low-energy gamma rays, X rays) from an  $^{241}\text{Am}$  source measured in air by the MiniPIX Timepix3 radiation camera equipped with a 500  $\mu\text{m}$  silicon sensor. A small portion of the detector pixel matrix is displayed (660  $\mu\text{m} \times 660 \mu\text{m} = 0.44 \text{ mm}^2 = 0.22\%$  of the entire sensor area). The per-pixel energy calibrated in keV is shown by the color bar. Deposited energy of single particles is indicated in keV [18].

## 2.3 Measurements

A total of 10 measurements at operational flight altitudes with different routes, dates and duration were used. The flights with a duration  $\leq 2$  hrs, were referred to as “short flights” and the other five flights with a duration  $\geq 7$  hrs were referred to as “long flights”. For these measurements the semiconductor pixel detector Timepix (tpx) described in Sec. 1.3 and the radiation camera MiniPIX (mpx) shown in Sec. 2.1 were used. The detector was prior per-pixel energy calibrated. It was operated in frame mode with acquisition time of 10 s. The detector sensor plane was oriented horizontally (i.e. parallel) or vertically (i.e. perpendicular) to the Earth horizon plane as shown in Figure 2.5.

The total elapsed time from the start of the measurements until the detector is turned off is the sum of the detector live time + detector dead time (approx 30 ms), as can be seen in Figure 2.4. The detector live time is the time interval in which the data is measured and is transferred to the computer system in the dead time.

Table 2.1 shows the measurement results and how the flights were classified.



Label	Date	Route	Route type	Live time [min]	Radiation camera/chip/SN
A	2022/09/04	PRG-BRUSS	SF	39	mpx/tpx/I10
B	2021/11/10	PRG-MOSCOW	SF	120	mpx/tpx/H09
C	2019/06/30	TOK-WARSAW	LF	401	mpx/tpx/I10
D	2019/06/16	WAR-TOK	SF	75	mpx/tpx/I10
E	2019/06/16	WAR-TOK-NP	LF	620	mpx/tpx/I10
F	2018/12/31	PARIS-TOK	LF	685	mpx/tpx/I10
G	2018/11/10	PRG-DUB.2	LF	815	mpx/tpx/I10
H	2018/11/10	PRG-DUB.3.1	SF	80	mpx/tpx/I10
I	2018/11/10	PRG-DUB.3.2	SF	115	mpx/tpx/I10
J	2018/11/10	PRG-DUB.3.3	LF	653	mpx/tpx/I10

Table 2.1: List of data of flights evaluated in this work. SF= short flight. LF=long flight. SN= Detector Serial Number. The frame acquisition time is 10 s. The flight altitudes were between 10 and 12 km.

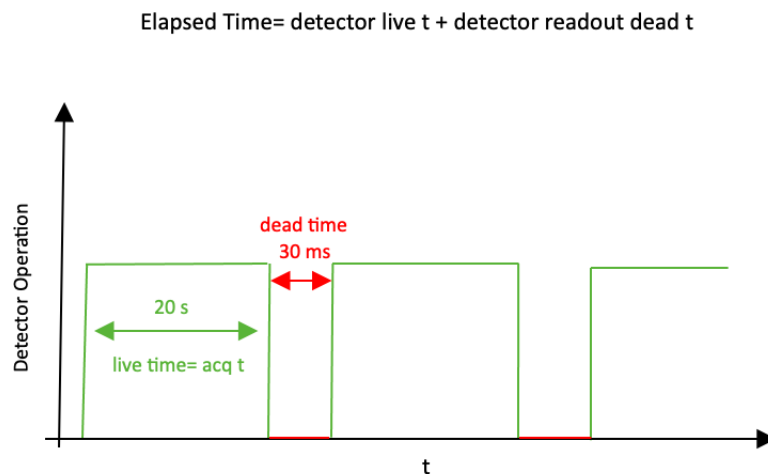


Figure 2.4: Illustration of the detector operation (Y axis) to the elapsed time (X axis). Total time = elapsed time = detector operation live time + detector readout dead time.

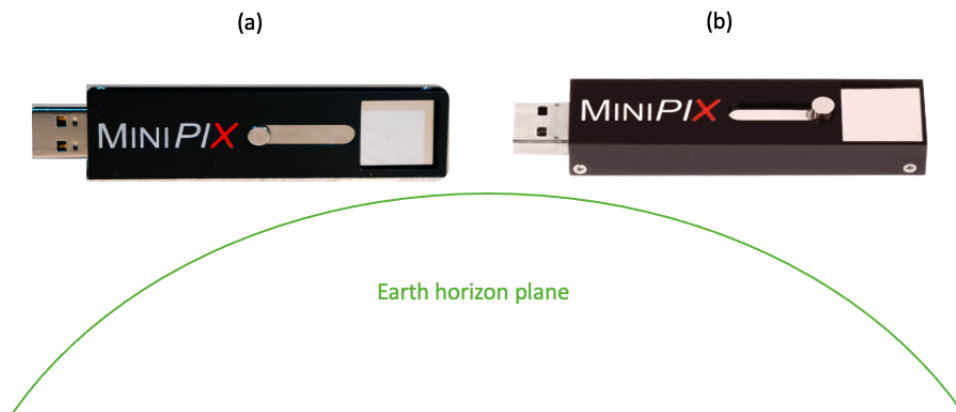


Figure 2.5: Illustration of the two possible geometries for positioning the detector with respect to the earth’s horizon line. (a) Vertical (perpendicular) or (b) horizontal (parallel).

## 2.4 Raw Data

Before processing, the “raw” data looks like in Figure 2.6. These files, with *.clog* extension, can be viewed in any modern text editor. Here the detailed list of clusters containing pixelated information is given. Each line that starts with “[” includes pixels of a cluster ( $[\mathbf{X}, \mathbf{Y}, \mathbf{E}] = [X \text{ position}, Y \text{ position}, \text{Energy}]$  of a pixel). This file includes all clusters and the mask or filters are not accounted for [19].

```

tot_clog
Frame 29 (1636538424.414669, 10.000000 s)
[206, 1, 46] [205, 2, 54] [207, 1, 42] [204, 2, 32]
[160, 201, 66] [159, 202, 83] [160, 202, 24] [158, 202, 41] [158, 203, 149] [157, 203, 41]

Frame 30 (1636538434.703316, 10.000000 s)
[226, 72, 98]

Frame 31 (1636538444.995889, 10.000000 s)
[202, 0, 52] [202, 1, 62] [202, 2, 182] [203, 2, 3] [202, 3, 26]
[18, 55, 148] [18, 56, 55] [19, 56, 90]
[210, 72, 15] [209, 73, 49] [210, 73, 44] [211, 72, 51] [208, 73, 37] [212, 72, 49] [207, 73, 55]
[206, 73, 30] [206, 74, 34] [205, 74, 61] [204, 74, 79] [203, 74, 55] [202, 74, 39] [202, 75, 41]
[201, 75, 53] [200, 75, 37]
[241, 112, 132] [240, 113, 97] [241, 113, 12] [239, 114, 49] [240, 114, 17]

Frame 32 (1636538455.284564, 10.000000 s)
[80, 68, 74]
[198, 159, 23] [197, 160, 137] [197, 161, 77] [196, 162, 45] [195, 163, 51] [196, 163, 45]
[152, 161, 61] [152, 162, 60] [152, 163, 37] [151, 164, 48] [152, 164, 16] [153, 164, 86] [151, 165,
106] [152, 165, 162] [153, 165, 67] [151, 166, 68] [151, 167, 59] [151, 168, 66] [151, 169, 47]
[50, 205, 16] [49, 206, 25] [50, 206, 83] [51, 206, 80] [51, 205, 52]
[143, 206, 27] [143, 207, 69] [143, 208, 92] [143, 209, 35]
[120, 233, 29] [120, 234, 119] [120, 235, 103]

Frame 33 (1636538465.573171, 10.000000 s)
[167, 56, 57] [166, 57, 64] [168, 56, 61] [165, 57, 54] [169, 56, 32]
[175, 124, 59] [175, 125, 84] [175, 126, 78] [175, 127, 60] [175, 128, 54]
[249, 126, 63] [250, 127, 51] [250, 126, 43] [251, 127, 101] [252, 128, 60] [252, 127, 68] [253, 128,
83]
[148, 146, 79] [148, 147, 42] [149, 147, 73] [149, 148, 45] [150, 148, 46] [150, 149, 52] [151, 149,
52]
[246, 165, 34] [246, 166, 7]

```

Figure 2.6: Example of raw data file. The data is collected in consecutive frames, with an acquisition time of 10 seconds, during which time single particles are registered.

Next to the frame number, in brackets, there is information about the time [i.g. Frame N (P, Q)=(UTC time, frame acquisition time)], both parameters are given in seconds

## 2.5 Data Processing

Data processing was performed using the software tool DPE (Data Processing Engine) provided by Advacam, which serves for processing of data acquired with the Timepix detectors (tpx, tpx2, tpx3) [19]. The main processing parts of the DPE are:

- **Pre-processing:** Data clustering with calibration and adjustments, calculation of cluster variables/parameters, and production of histograms
- **Processing:** Particle and radiation field recognition
- **Post-processing:** Directional analysis, coincidence analysis, Compton camera, physical product production (fluxes, dose rates, deposited energy, etc) and time evolution in relation to radiation field classification

### 2.5.1 Pre-Processing

This stage provides conversion of pixelated data into groups of correlated pixels, named clusters. The level of correlation is determined by the detector used to collect data. In the case of the Timepix detector, only spatial correlation is provided, which is then used in the clusterization process. At this stage a main energy per pixel calibration, to convert digital time-over-threshold (ToT) information to energy in keV, is applied. This approach is accompanied by additional calibrations and corrections aimed at suppressing detector undesired or abnormal behavior to the greatest extent possible. The clusterization stage is followed by cluster analysis, which examines the morphological and spectral properties of the clusters [19]. In summary, what is done at the pre-processing stage is:

- **Clustering:** Grouping pixels based on coordinates and, if available, time information.
- **Calibration and corrections:** Energy calibration, cluster size and tpx

high energy correction, etc.

- **Cluster parameters:** Calculation of overall cluster parameters.

## 2.5.2 Processing

To process the data, several parameters must be configured, the most important are:

- File path to be processed.
- Sampling time (time for data sampling in seconds).
- Select the type of detector chip (i.e. tpx, tpx2, tpx3) used for the measurement.
- Sensor material of the detector (i.e. Si, CdTe, GaAs).
- Thickness, in  $\mu\text{m}$ , of the detector (i.e. 100  $\mu\text{m}$ , 300  $\mu\text{m}$ , 500  $\mu\text{m}$ ).
- Path to the calibration matrices (provided by DPE software) according to the detector characteristics.

Particle recognition, cluster analysis parameters and radiation field recognition is made at this stage. Results from DPE are exported into several directories separated in most cases based on the type of the analysis [19].

As an output of this stage, a text file named *Elist* is created, which contains the cluster variables/parameters such as: DetectorID, EventID, X position (mm), Y

position (mm), Energy (keV), Time (s), Size (px), Angle (rad), etc. The Figure 2.7 shows a part of the Elist file of measurement **B** described in Table 2.1.

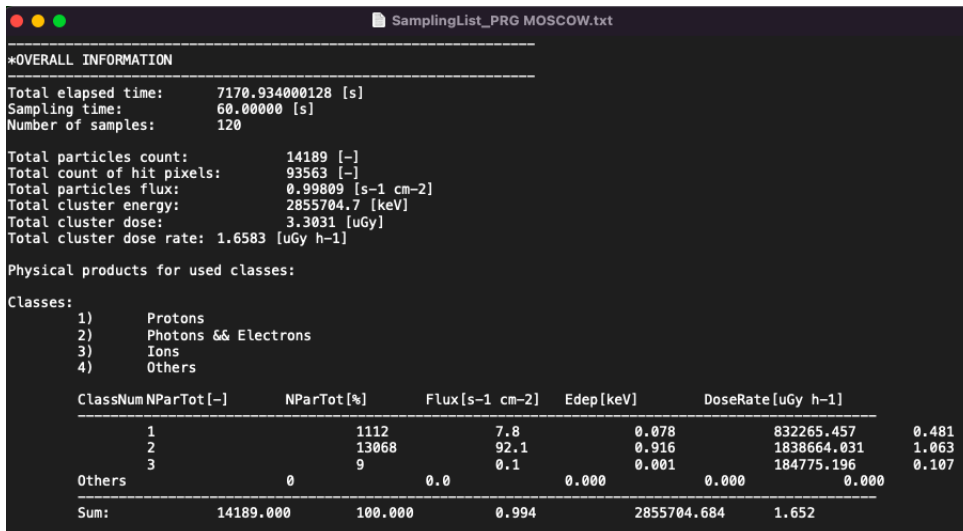
```

DetectorID;EventID;x;y;E;t;Flags;Size;Height;BorderPixCount;Roundness;Angle;Linearity;Length;Width
-;-;mm;mm;keV;s;-;px;keV;-;-;rad;-;px;px
0;0;7.37;3.41;48.5297;1636538136.289;0;1;48.5297;1;1;0;1;0;0
0;0;8.66849;12.4243;110.431;1636538136.289;0;7;28.0121;7;0.697891;1.27476;0.690461;4.11773;1.24823
0;0;10.157;6.435;44.1528;1636538136.289;0;2;29.7073;2;1.18587;0;1;1;0
0;0;6.27;6.325;17.6837;1636538136.289;0;1;17.6837;1;1;0;1;0;0
0;0;4.28222;13.1933;81.0829;1636538146.582;0;4;54.1775;4;0.918384;0.36482;0.577842;2.22516;0.934188
0;0;10.246;11.7031;133.709;1636538146.582;0;9;24.2279;9;0.428656;-0.966972;0.873993;7.2102;0.880213
0;0;12.0899;10.2508;191.045;1636538156.868;0;5;72.8547;5;0.694397;-0.708886;0.69602;2.82015;0.867186
0;0;3.57911;7.63052;299.171;1636538167.157;0;9;81.1645;9;0.535335;0.031036;0.764845;5.02862;1.15467
0;0;7.68123;13.6013;334.606;1636538177.452;0;3;220.443;3;1.01418;-0.732034;0.771955;1.4122;0.743816
0;0;0.902823;13.64;32.0715;1636538177.452;0;2;18.7632;2;1.36381;0;1;1;0
0;0;5.78315;0.03946;87.8034;1636538177.452;0;4;51.1238;4;1.0554;0.926719;0.227712;1.40012;1.40012
0;0;2.23549;7.63011;193.099;1636538177.452;0;7;67.0204;7;0.970216;-0.932844;0.438541;2.79774;1.99442
0;0;1.06441;4.58441;114.491;1636538177.452;0;4;31.9239;4;0.484436;0.785398;1;4.24264;7.77156e-16
0;0;12.43;8.39277;77.6777;1636538187.740;0;2;46.2875;2;1.33897;1.5708;1;1;6.12323e-17
0;0;5.19363;1.2388;349.413;1636538187.740;0;21;28.847;21;0.272337;1.42079;0.88762;18.2462;2.21908
0;0;9.02;0.055;55.289;1636538198.029;0;1;55.289;1;1;0;1;0;0
0;0;1.375;11.5121;113.25;1636538198.029;0;3;50.4251;3;0.745625;1.5708;1;2;1.22465e-16
0;0;5.99809;8.21196;111.429;1636538198.029;0;6;23.155;6;0.637061;-0.260821;0.808786;4.12259;0.966179
0;0;4.37244;7.18891;106.438;1636538198.029;0;8;23.7299;8;0.614439;0.214605;0.741341;5.09826;1.19002

```

Figure 2.7: Elist data file of processed single particles (listed in rows) each with detailed imaging, spectral and tracking values (listed in columns) of measurement **B** described in Table 2.1.

Another important output file obtained is the *Sampling List* file. It includes basic information about the radiation field and their time dependency. This file includes both the information of all detected particles summed up and separated by class (protons, photons and electrons, ions and others). In the sampling list the total elapsed time, particles count, particles flux, cluster energy and dose rate can be found. A portion of the sampling list file is shown in Figure 2.8.



```

*OVERALL INFORMATION
-----
Total elapsed time: 7170.934000128 [s]
Sampling time: 60.00000 [s]
Number of samples: 120

Total particles count: 14189 [-]
Total count of hit pixels: 93563 [-]
Total particles flux: 0.99809 [s-1 cm-2]
Total cluster energy: 285704.7 [keV]
Total cluster dose: 3.3031 [uGy]
Total cluster dose rate: 1.6583 [uGy h-1]

Physical products for used classes:
Classes:
1) Protons
2) Photons & Electrons
3) Ions
4) Others

ClassNum NParTot [-] NParTot [%] Flux[s-1 cm-2] Edep[keV] DoseRate[uGy h-1]
-----
1 1112 7.8 0.078 832265.457 0.481
2 13068 92.1 0.916 1838664.031 1.063
3 9 0.1 0.001 184775.196 0.107
Others 0 0.0 0.000 0.000 0.000
Sum: 14189.000 100.000 0.994 285704.684 1.652

```

Figure 2.8: Sampling list file of measurement **B** described in Table 2.1. The sampling list file evaluates the physical quantities of the radiation field measured (particle fluxes, dose rates, deposited dose) in fixed time intervals e.g., 1 min.

### 2.5.3 Post-Processing

The post-processing is where the physics data is produced. The main information found in the exported files can be summarized as follows:

- Flux
- Dose Rate
- Deposited Energy
- Distributions of cluster variables
- LET spectra

All time-coupled variables in the output sampling list are calculated with respect to the sampling time of each flight. Total variables are calculated in relation to the elapsed time, which is typically shorter [19].



# Chapter 3

## Results

This section presents detailed results, mainly of measurements **B** and **G** described in Table 2.1. The data were collected with the radiation camera MiniPIX-Timepix previously described in Section 2.1, which is equipped with the 300 [ $\mu\text{m}$ ] Silicon sensor.

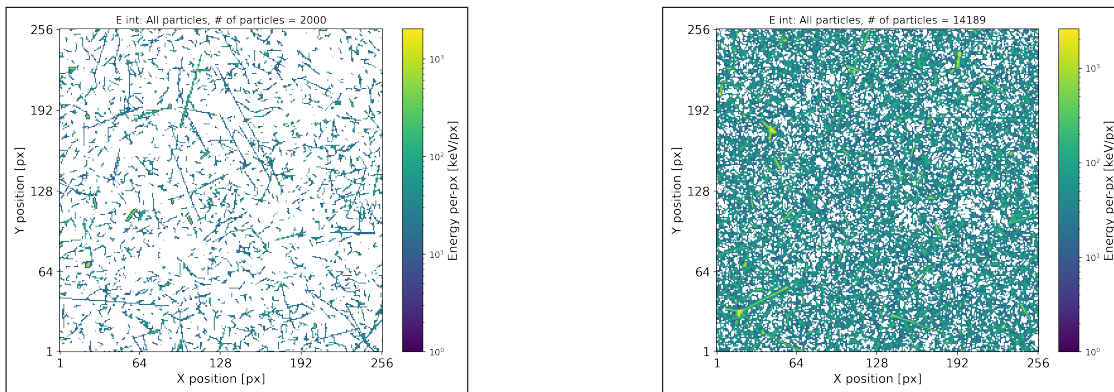
The results are organized and presented according to the information and physics data products obtained. Detection and quantum-imaging visualization of the radiation fields measured inside an aircraft at flight altitudes are given in Sec. 3.1. Analysis and results of the composition characterization of the radiation fields are shown in Sec. 3.2. The event count rates of the two flights for all detected particles, and according to particle event, is given in Sec. 3.3. The particle fluxes, deposited energy and dose rates for flights **B** and **G** as well as for the rest of the flights described in Table 2.1 are shown in Sections 3.4, 3.5, 3.6, respectively.

### 3.1 Detection and visualization of radiation field

Single particles are detected as energy-sensitive tracks called *clusters*. The per-pixel deposited energy is shown in Figures 3.1, 3.2 in the color scale (in keV/px, log scale). The entire detector pixel matrix is displayed, that is, 256 x 256 pixels = 14.1 mm x 14.1 mm = 1.98 cm<sup>2</sup> = 65 k pixels.

Figure 3.1 shows the first 2k integrated tracks of flight **B** measured in an interval of approximately 16.8 min.

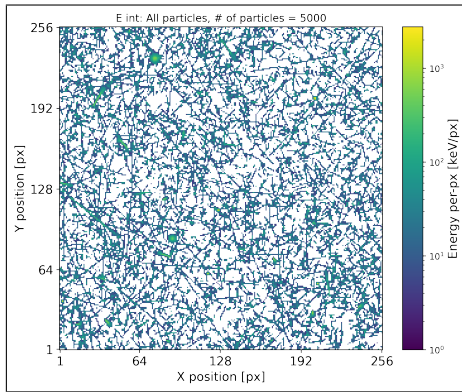
Figure 3.2 shows all integrated tracks (14189), measured in the total elapsed time (detector live time + dead time) which is 119.8 min for that flight.



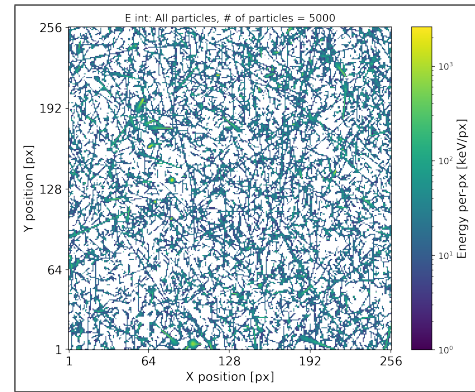
(a) First 2k clusters.

(b) All clusters: 14189.

Figure 3.1: Detection and track visualization of the mixed-radiation field produced during the short flight: **B** (see Table 2.1) inside commercial aircraft at operational flight altitudes (10 km). The deposited energy, measured per pixel, is displayed by the color scale. All detected particles are displayed. A total of (a) 2k tracks collected in many frames over 17 minutes and (b) 14189 tracks collected during the whole flight (2 hours) are displayed as a single integrated frame.



(a) First part of the measurement (5k to 10k clusters).



(b) Last part of the measurement (40k to 45k clusters).

Figure 3.2: Similar to Figure 3.1 for data from a long flight:  $\mathbf{G}$  (see Table 2.1). Integrated data show (a) 5 k tracks measured in 77 min at the beginning of the flight, and (b) also 5 k tracks measured in the last 77 minutes of the flight.

## 3.2 Composition characterization

There is information contained in the morphology and per-pixel spectrometry depending on the particle type, spectra response (energy loss) and direction of incidence to the detector sensor plane [5].

Single particles generate signals in the pixelated semiconductor sensor that involve many pixels forming a cluster of pixels. The charge sharing effect and the convolution of the deposited charge along its course produce the pattern and morphology of the pixel clusters. High-resolution micro-scale pattern recognition algorithms examine the individual particle tracks with the aim of identifying particle types [14].

If we take a look at Figure 2.2, distinct particle tracks can be easily identified (by its size, length and thickness). It is possible to resolve several sorts of events through analysis of the distinctive tracks in the pixel matrix. The particle type, energy, and direction are all important factors that affect the morphology and spectrum distribution of the deposited energy [14].

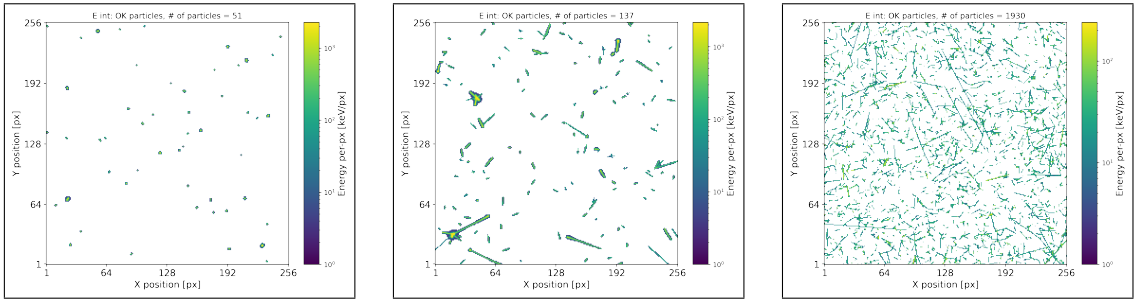
Large tracks with high per-pixel energy are formed by heavy charged particles of high energy and non-perpendicular direction, or low energy and perpendicular incident direction. Small tracks of few pixels and low per-pixel energy are produced by X rays. Thin curly tracks of varying size and morphology and small per-pixel energy are produced by electrons and gamma ray interactions [5].

Taking this into account, the tracks were filtered into 3 different classes as shown in Table 3.1.

Class	Selected Particles Description
<b>a</b>	Low-energy and/or perpendicular high-let HCPs, namely protons.
<b>b</b>	High-energy and/or non-perpendicular high-let HCPs, namely protons.
<b>c</b>	Low-let LCPs, namely electrons, X rays, gamma rays, muons.

Table 3.1: Particle classification into three main groups according to their energy, direction and morphology.

The radiation fields shown in Figure 3.1 and 3.2 were filtered as we can see in the following figures.

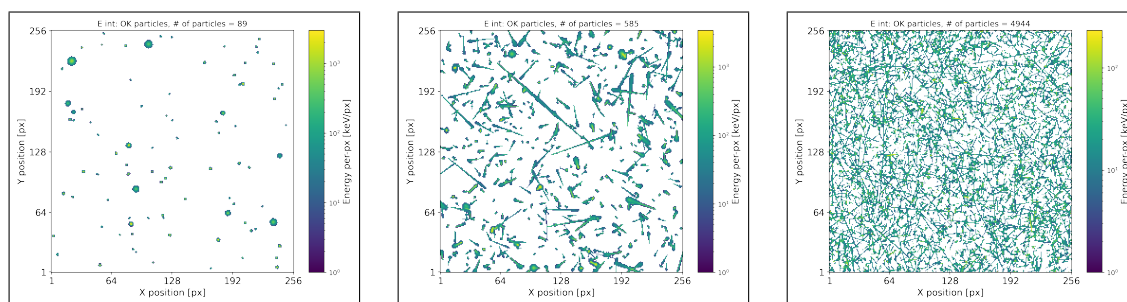


(a) Class **a** for the whole measurement.

(b) Class **b** for the whole measurement.

(c) Class **c** for the first 2k clusters.

Figure 3.3: Plot of integrated tracks of selected particles for short flight **B**. Similar to Figure 3.1 showing the selected particle-event types: (a) class **a** for the whole measurement, (b) class **b** for the whole measurement and (c) class **c** for 2k clusters. See Table 3.1.



(a) Class **a** for the whole measurement.

(b) Class **b** for the whole measurement.

(c) Class **c** for the first part of the measurement.

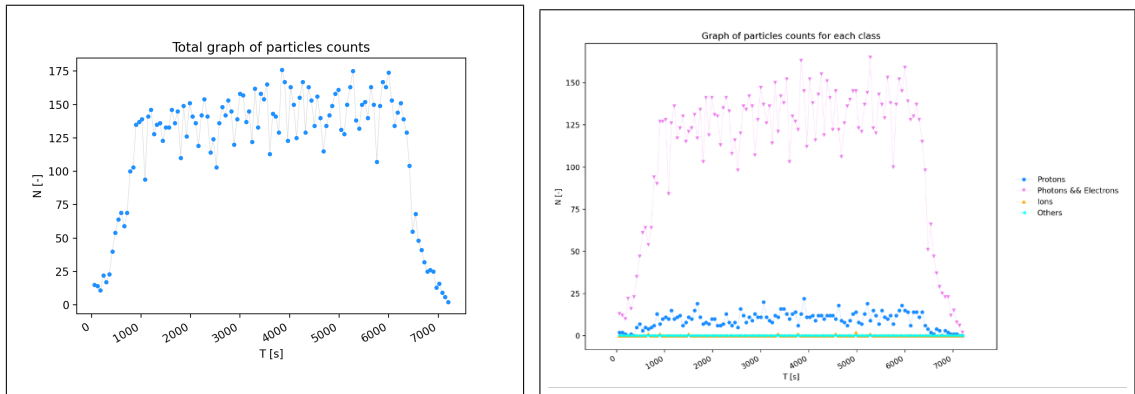
Figure 3.4: Similar to Figure 3.3. Plot of integrated tracks of selected particles for long flight **G**.

The protons exhibit high energy loss and are thus characterized by large tracks of high per pixel energy. Such large wide tracks can be seen in the integrated data in Figure 3.3b and 3.4b. The electrons, X rays and gamma rays, on the contrary, exhibit low energy loss and produce small and narrow tracks in the detector of characteristic small per pixel energy. Such tracks appear as narrow long tracks in the detector as can be seen in Figure 3.3c and 3.4c. Protons with low per-pixel energy, and characterized by round tracks, are shown in Figure 3.3a and 3.4a.

From Figure 3.3 and 3.4 it can be seen that particles of classes **a** and **b** are the least detected compared to class **c** particles which, in a short fragment of the measurement, were detected more than for the other two classes in the whole measurement.

### 3.3 Event count rates

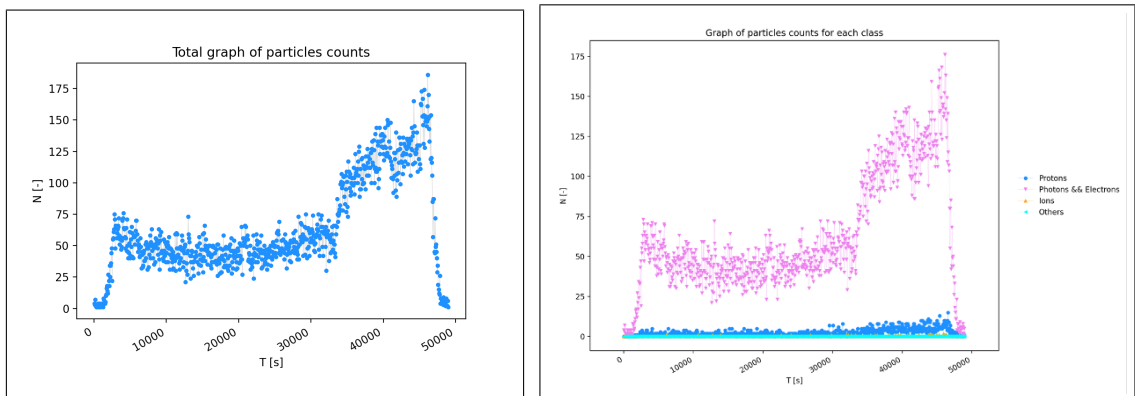
Figure 3.5 shows the number of particles detected per second of flight **B** described in Table 2.1, same for Figure 3.6 but for long flight **G**.



(a) Particle event count rates, all particles.

(b) Particle event count rates, according to particle class.

Figure 3.5: Particle event count rates for the whole measurement for short flight **B**.



(a) Particle event count rates, all particles.

(b) Particle event count rates, according to particle class.

Figure 3.6: Particle event count rates for the whole measurement for long flight **G**.

The number of incident events increases after the first few minutes of flight as can be seen in Figure 3.5 and 3.6. This can be read as the airplane taking off and gaining altitude, as there are more particles observed than on the ground. The same can be said for the last minutes of the flights, when descending to the ground, the ionizing radiation also decreases. Figure 3.6 shows an increment in charge particles detected between about 35k-45k seconds, these variations can be interpreted as an increase in flight altitude or changes in cosmic rays flux over long distances.

According to particle class, photons and electrons are the particles with the highest incidence detected, heavy charged particles such as protons were detected in smaller quantities. Finally, particles such as ions were detected but in almost nil quantities. Table 3.2 shows the number of protons, photons, electrons and ions detected during the sampling time of flights **B** and **G** described in Table 2.1.

Label	Protons		Photons and Electrons		Ions		Total particles	
	(#)	(%)	(#)	(%)	(#)	(%)	(#)	(%)
<b>B</b>	1112	7.8	13068	92.1	9	0.1	14189	100
<b>G</b>	1917	3.7	50488	96.3	36	0.1	52441	100

Table 3.2: Number and percentage of each particle class detected on flights **B** and **G** from the Sampling list obtained in the post-processing stage.

We can see that for flight **B** there is 7.8% and for flight **G** a 3.8% of the total detected particles which are HCPs. The rest are photons and electrons.



### 3.4 Particle fluxes

The radiation field can be evaluated in terms of particle flux with particle-type composition sensitivity [5]. The flux of a quantity is defined as the rate at which this quantity passes through a fixed boundary per unit time. In this case, we are interested in knowing the flux of the different types of particles that have been detected during the flight. The flux can be obtained by normalizing the event count rate to sensor area ( $1.98 \text{ cm}^2$ ) per unit time.

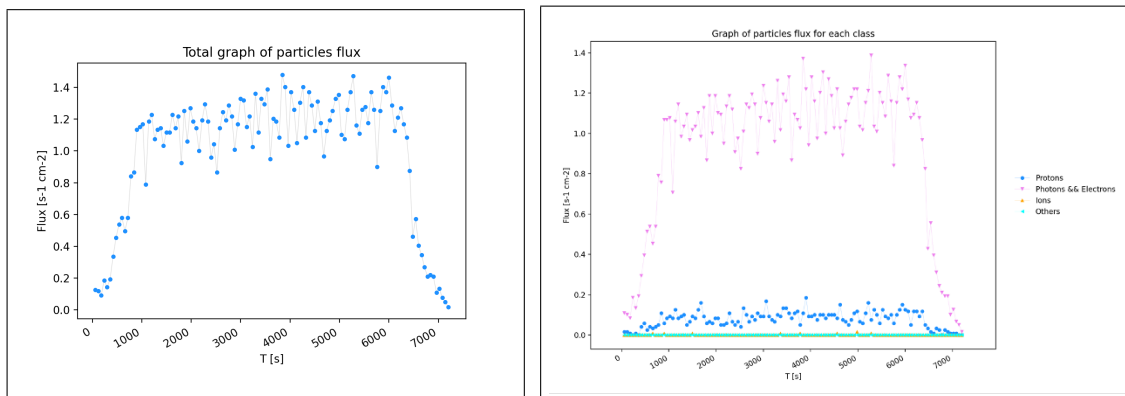
Table 3.3 shows the total particle count, measured live time displayed in minutes and the total flux for each measurement described in Table 2.1.

Label	Particles count(#)	Measured live time (min)	Flux ( $\#/\text{min}/\text{cm}^2$ )
<b>A</b>	3616	38.94	46.9
<b>B</b>	14189	119.82	59.8
<b>C</b>	47421	400.2	59.7
<b>D</b>	3974	76.09	25.4
<b>E</b>	83752	620.07	68.2
<b>F</b>	86577	685.97	63.7
<b>G</b>	52441	814.78	32.5
<b>H</b>	4728	80.88	29.5
<b>I</b>	9350	113.83	41.5
<b>J</b>	44906	651.82	34.8

Table 3.3: Total particle count, measured live time and flux for each measurement

### 3.4.1 Selected flights

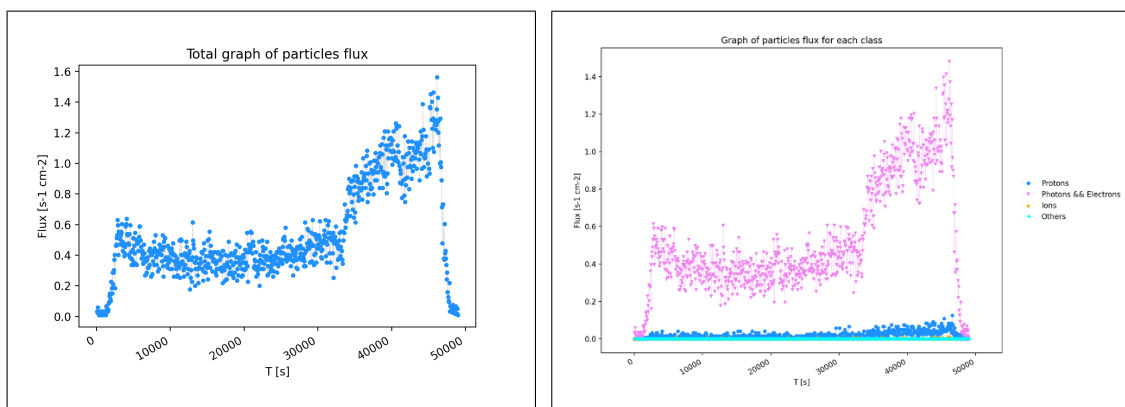
Figure 3.7a and 3.8a present the particle flux of all types of particles for the two flights previously described and Figures 3.7b and 3.8b show the flux by particle class.



(a) Particle flux, all particles.

(b) Particle flux, according to particle class.

Figure 3.7: Flux for the whole measurement for short flight **B**.



(a) Particle flux, all particles.

(b) Particle flux, according to particle class.

Figure 3.8: Flux for the whole measurement for long flight **G**.

As can be seen, photons are the type of particle with the highest incidence,

which is not surprising as we saw it in the previous section.

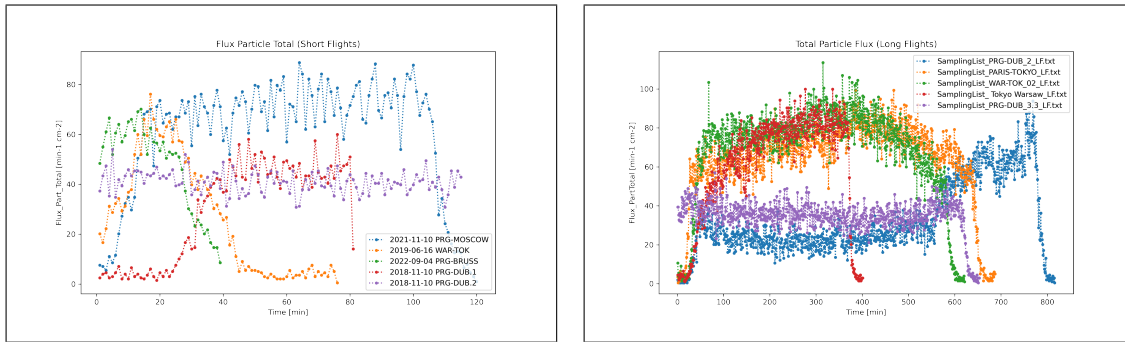
<b>Label</b>	<b>Protons flux</b> (#/min/cm <sup>2</sup> )	<b>Photons and Electrons flux</b> (#/min/cm <sup>2</sup> )	<b>Ions flux</b> (#/min/cm <sup>2</sup> )	<b>Total particles flux</b> (#/min/cm <sup>2</sup> )
<b>B</b>	4.68	55	0.04	59.72
<b>G</b>	1.19	31.25	0.02	32.46

Table 3.4: Particle flux by class of flights **B** and **G** obtained from the Sampling list in the post-processing stage.

For obtaining the particle fluxes showed in Table 3.4, the total number of particles detected (by class) is divided by the sampling time in minutes of each flight and for the sensor area.

### 3.4.2 All flights

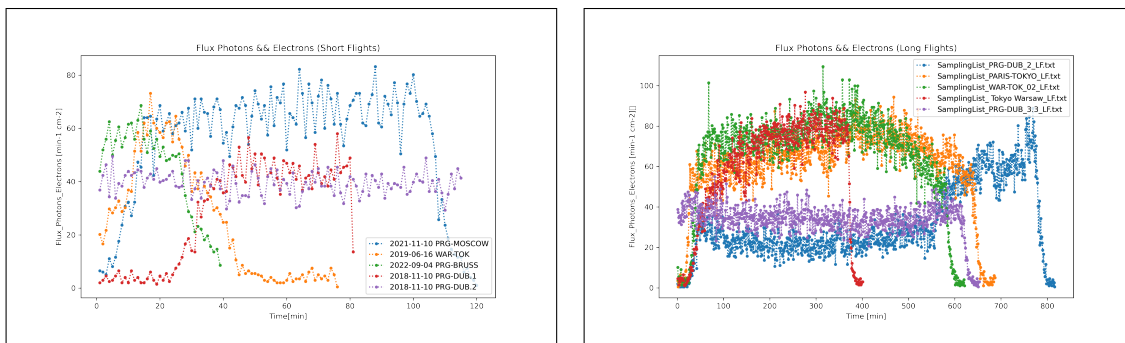
The particle fluxes of all flights in Table 2.1 were compared. Plots of the flux of all particles detected and selected particles in short and long flights are presented in Figure 3.9 and 3.10.



(a) Particle flux, all particles, short flights:  
**A,B,D,H,I.**

(b) Particle flux, all particles, long flights:  
**C,E,F,G,J.**

Figure 3.9: Flux for the whole measurement for all short and long flights described in Table 2.1.



(a) Particle Flux, Photons and Electrons,  
Short Flights.

(b) Particle Flux, Photons and Electrons,  
Long Flights.

Figure 3.10: Photons and electrons flux for the whole measurement for all short and long flights described in Table 2.1.

From Figure 3.9a and 3.10a it can be concluded that the short flight with the highest particle flux and, therefore, with the highest radiation was flight **B**; from Figures 3.9b and 3.10b it can be said that the long flights with the highest radiation were flights **E** and **F**, which makes sense since both flights had the same destination (see Table2.1).

## 3.5 Deposited Energy

The deposited energy (DE) is described as the amount of energy deposited by ionizing radiation in a material per unit mass of the material [20].

### 3.5.1 Time distribution

Figure 3.11 and 3.12 show the deposited energy (measured in keV per time) of the selected flights **B** and **G** described in Table 2.1. The DE of all particles detected and then separated by particle class is shown.

Figure 3.13, 3.14 and 3.15 show the deposited energy of all particles, protons and photons respectively of all short and long flights described in Table 2.1.

#### Selected Flights

In Figure 3.11 and 3.12, the x-axis, which corresponds to the time in seconds, only takes into account the live-time of the detector, it does not include the detector readout dead-time which is negligible anyway (30 ms in comparison to 10 s which is the frame acquisition time).

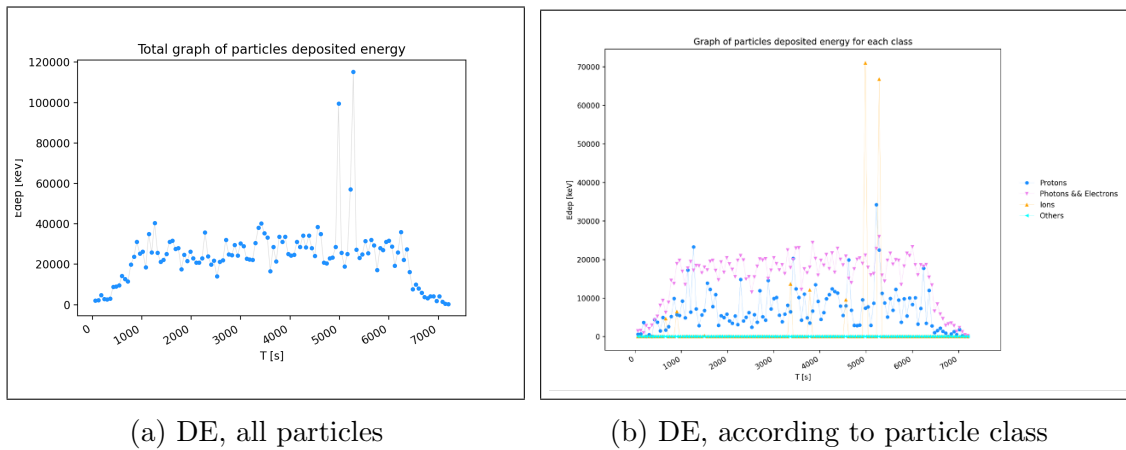


Figure 3.11: Deposited energy for the whole measurement for short flight **B**, measured in keV per second.

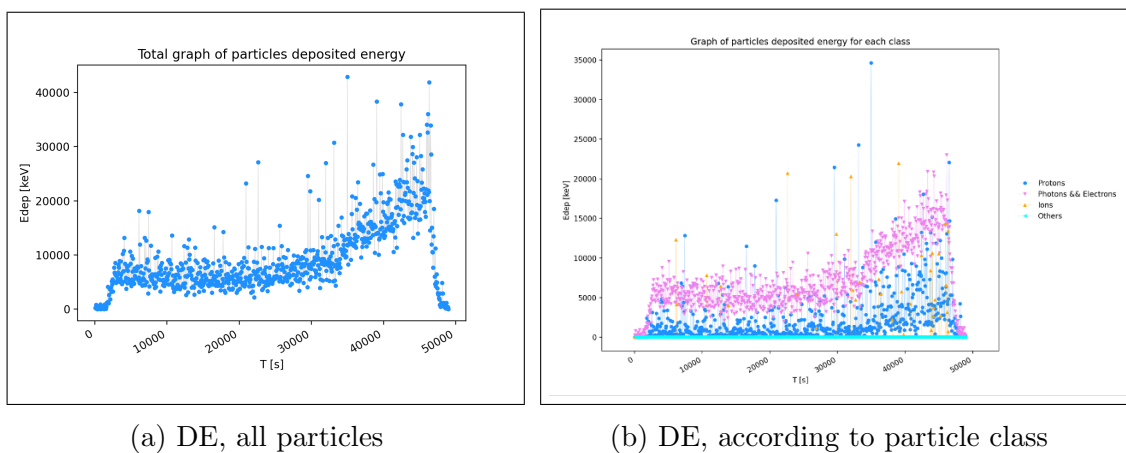


Figure 3.12: Deposited energy for the whole measurement for long flight **G**, measured in keV per second.

As it was seen in Sec. 3.3 and 3.4, photons and electrons contribute the highest particle count. However, the presence of protons and ions (HCPs) is notably limited. In Figure 3.11b and 3.12b, we can see the distribution of deposited energy depending on the particle type and it can be noticed that, despite the relatively low abundance of protons and ions, their cumulative deposited energy constitutes

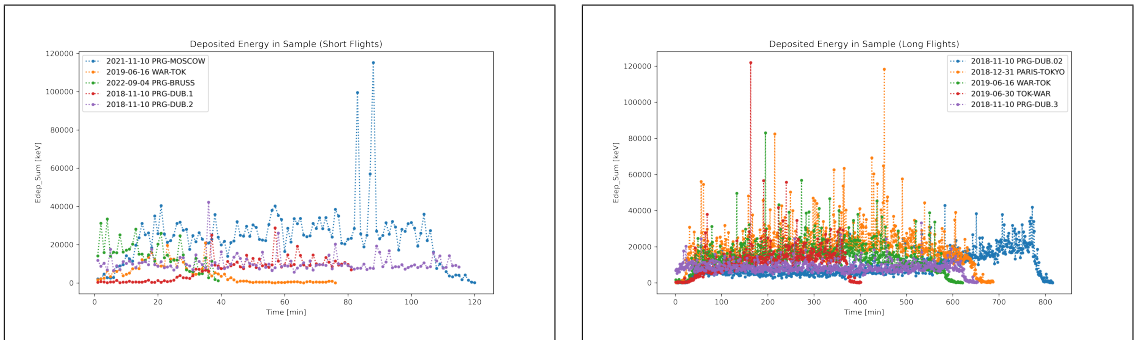
a substantial component of the overall deposited energy (DE). Table 3.5 shows the average of deposited energy by particle class (protons, photons/electrons and ions).

Label	DE by protons (keV)	DE by photons and electrons (keV)	DE by ions (keV)	Average DE (keV)
<b>B</b>	6935.5	15322.2	1539.8	23797.5
<b>G</b>	2025.6	7069.3	310.56	9405.5

Table 3.5: Deposited energy average in keV by particle class during the sampling time in minutes for measurements **B** and **G** described in Table 2.1.

## All Flights

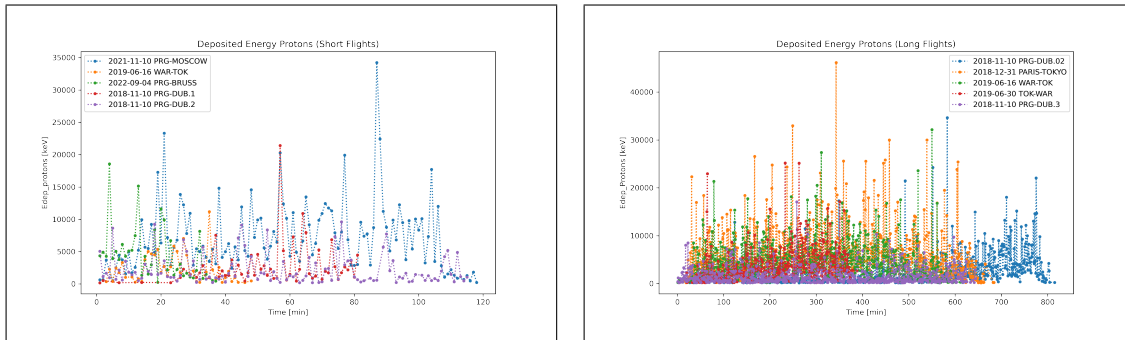
Deposited energy plots were generated for all particles and the different particle types as can be seen in Figure 3.13, 3.14 and 3.15. The measurements were categorized into short flights (SF) and long flights (LF), as detailed in Table 2.1 for an easier comparison.



(a) Deposited energy, all particles, short flights: **A,B,D,H,I**.

(b) Deposited energy, all particles, long flights: **C,E,F,G,J**.

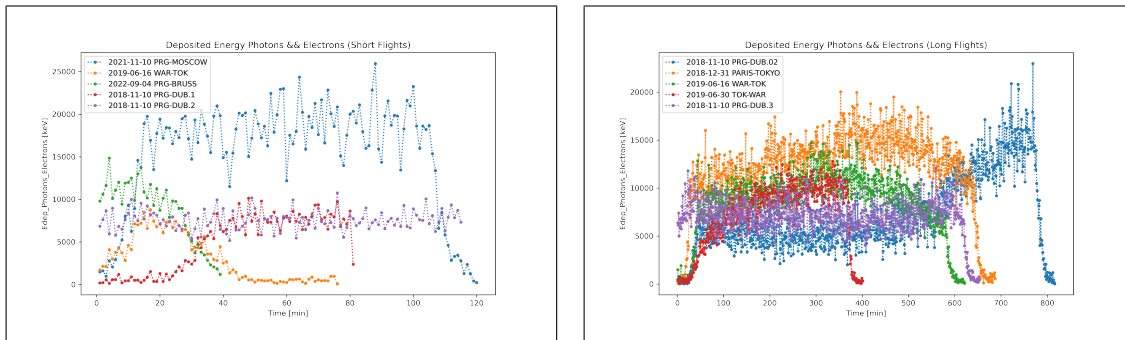
Figure 3.13: Total deposited energy for the whole measurement for all short and long flights described in Table 2.1, measured in keV per minute.



(a) Deposited energy, protons, short flights: **A,B,D,H,I**.

(b) Deposited energy, protons, long flights: **C,E,F,G,J**.

Figure 3.14: Deposited energy of protons for the whole measurement for all short and long flights described in Table 2.1.



(a) Deposited energy, photons and electrons, short flights: **A,B,D,H,I**.

(b) Deposited energy, photons and electrons, long flights: **C,E,F,G,J**.

Figure 3.15: Deposited energy of photons and electrons for the whole measurement for all short and long flights described in Table 2.1.

It can be observed, from Figure 3.14a and 3.14b, that although the deposited energy by protons has certain peaks that exceed the 30000 or 40000 keV per minute, on average, photons and electrons are the particles that deposit the most energy during the flight (See also Figure 3.15a and 3.15b). Likewise it can be said, from Figure 3.13, that the short flight with the highest deposited energy was flight **B**, and the long flights with the highest DE were flights **E** and **F**. Same as



observed in the previous section.

### 3.5.2 Deposited Energy Spectra

The Timepix detector can measure the deposited energy by any particle.

In Figure 3.16 the deposited energy spectra with all particles displayed can be seen. At the top of the following images, a linear axis is used while a logarithmic axis is used at the bottom.

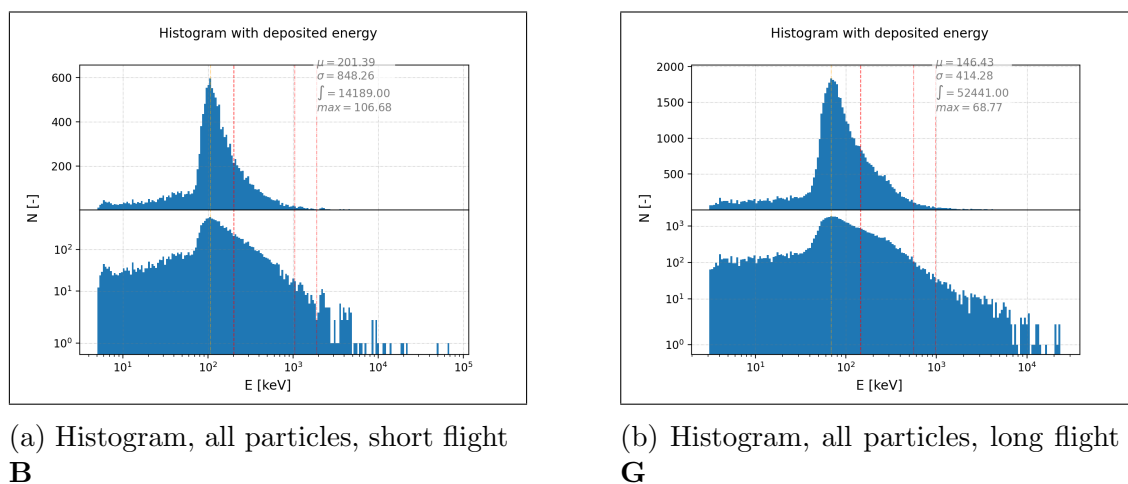


Figure 3.16: Deposited energy spectra of flights **B** and **G** described in Table 2.1.

As can be seen, the deposited energy spectrum is wide, it cover ranges from a few keV up to MeV level. The hard part of the spectrum is slightly above 100 keV, which is deposited mostly by protons and HCPs. The soft part of the spectrum, on the other hand, is below 100 keV; this part is produced by LCPs, electrons, X rays and gamma rays. The energy distribution is quite similar between the two figures with the difference that less particles were detected in the short flight **B**

than in the long one **G**.

## 3.6 Dose rates

The absorbed dose is obtained as the ratio  $d\varepsilon/dm$ , where  $d\varepsilon$  is the average energy deposited by radiation to a material of mass  $dm$ :

$$D = \frac{d\varepsilon}{dm}.$$

The absorbed dose rate (DR) is defined as the rate  $dD/dt$  where  $dD$  is the increase in absorbed dose during the time interval  $dt$ :

$$DR = \frac{dD}{dt}.$$

Dose rate is often indicated in micro grays per hour [ $\mu Gy/h$ ].

### 3.6.1 Selected flights

Figure 3.17 and 3.18 show the resultant dose rate ( $\mu Gy/h$ ) throughout flights **B** and **G**, described in Table 2.1. The dose rate obtained from all particles is shown in Figure 3.17a and 3.18a and then separated by class in Figure 3.17b and 3.18b, where it can be seen that photons and electrons are the particles that deposit the highest dose rate followed by protons.

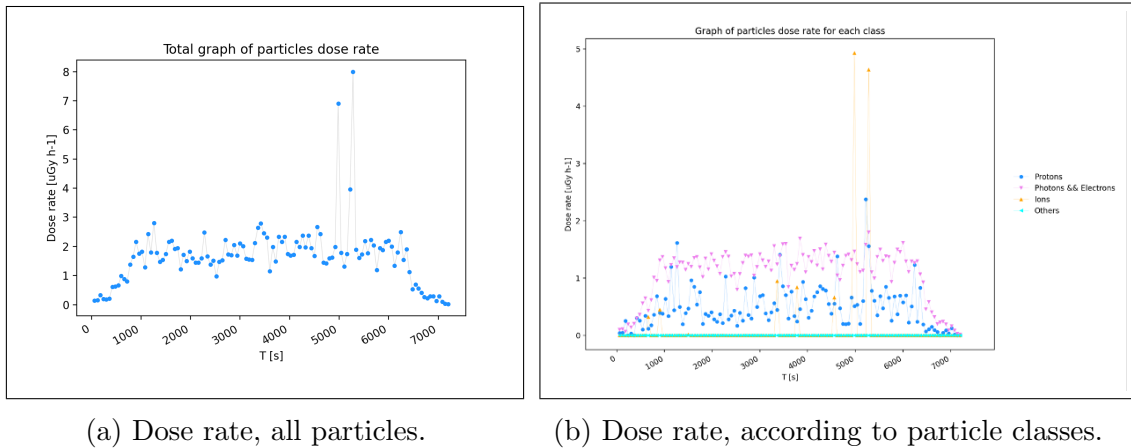


Figure 3.17: Dose rate for whole measurement for short flight **B**.

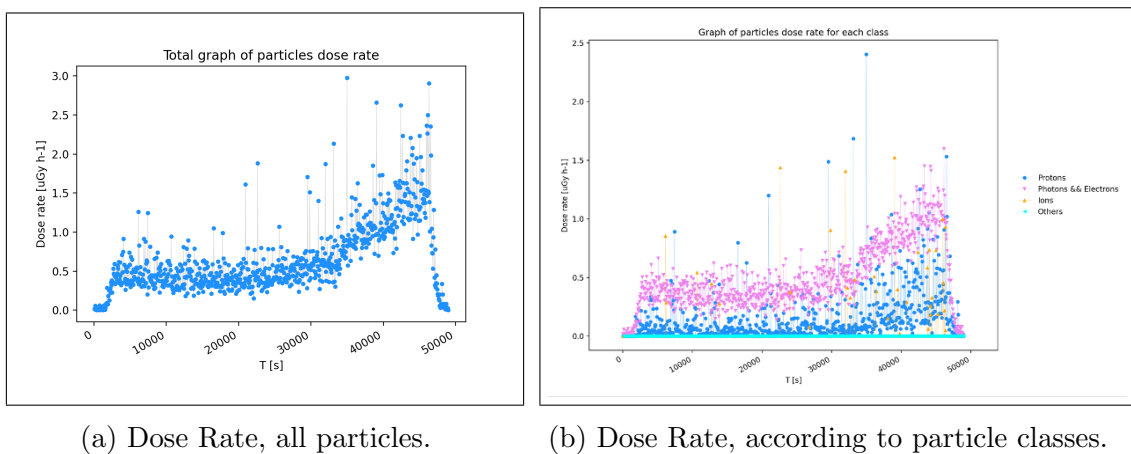
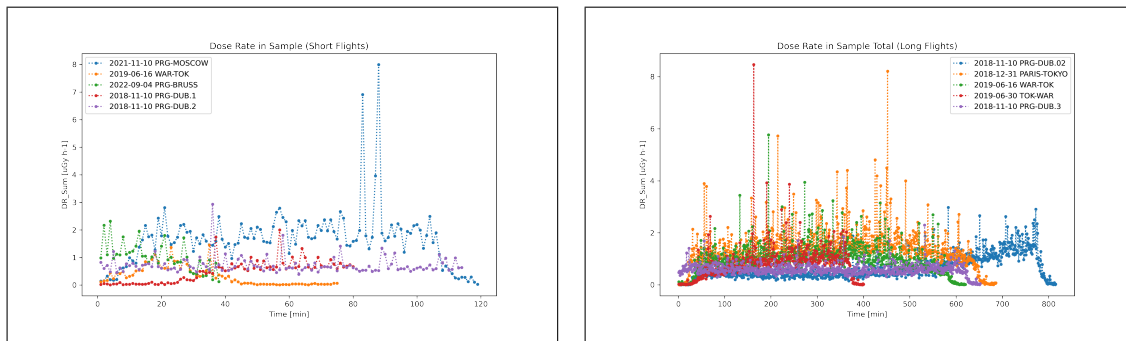


Figure 3.18: Dose rate for whole measurement for long flight **G**.

Generally, the dose rate in the first and last seconds of flight is expected to be low. In Figure 3.18 we can see a small variation in the last minutes of the flight, which can reflect changes in the cosmic rays flux over long distances. Fluctuations of small duration, which can significantly increase the dose rate in a short time interval during the flight, also occur.

### 3.6.2 All flights

Figure 3.19 shows the dose rate of all particles for all flights described in Table 2.1



(a) Dose Rate, all particles, short flights **A,B,D,H,I**.

(b) Dose Rate, all particles, long flights **C,E,F,G,J**.

Figure 3.19: Dose rate for the whole measurement for (a) short and (b) long flight described in Table 2.1.

From the Figure 3.19 it can be said that the short flight with the highest dose rate was flight **B**, and the long flights with the highest DR were flights **E** and **F**. Similar to what was observed in Sec. 3.4 and 3.5.

It also can be seen that, in general, the dose rate is low at ground level (at the beginning of the measurement) up to a few km altitude (data taken a few minutes after the plane took off) and then it increases above 3 to 4 km, usually. In long flights, small variations (see blue data in Figure 3.19b), which can be interpreted as changes in the cosmic rays flux over long distances, can be seen.

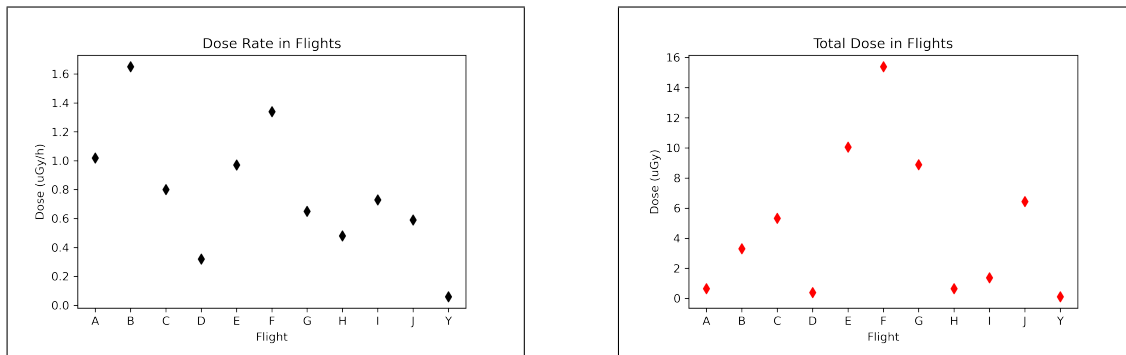
### 3.7 Dose

Given the dose rate and the sampling time of each measurement, the total detected dose that the aircraft and passengers received during the measurement time can be calculated.

Table 3.6 shows the different flights with its detection time in hours, the average dose rate in ( $\mu\text{Gy/h}$ ), the calculated dose given in ( $\mu\text{Gy}$ ) and the standard deviation of each flight data. To compare the measurements as a function of altitude, two new data (Y,Z) have been added. The **Y** label refers to the measurement on ground (Prague) with the same detector as the previous flights, and the **Z** label is the measurement in LEO orbit onboard Proba-V satellite [21], approximately at 830 km altitude. These data were obtained from Table 1 in [5] and Table 3 in [21], respectively.

Label	Time (h)	Average Dose Rate ( $\mu\text{Gy/h}$ )	Dose ( $\mu\text{Gy}$ )	Standard Deviation
<b>A</b>	0.65	1.02	0.66	0.53
<b>B</b>	2	1.65	3.3	1.06
<b>C</b>	6.68	0.8	5.33	0.66
<b>D</b>	1.27	0.32	0.4	0.34
<b>E</b>	10.35	0.97	10.06	0.58
<b>F</b>	11.45	1.34	15.39	0.75
<b>G</b>	13.6	0.65	8.88	0.46
<b>H</b>	1.35	0.48	0.65	0.4
<b>I</b>	1.9	0.73	1.38	0.31
<b>J</b>	10.88	0.59	6.44	0.22
<b>Y</b>	2	0.06	0.12	
<b>Z</b>	1	3360	3360	

Table 3.6: Dose rate, Total Dose and Standard Deviation during each flight described in Tab. 2.1. Y is the ground dose in 2 h at 200 m altitude in Prague. Z is the dose given by the satellite (Proba-V) in 1 h at 820 km altitude.



(a) Average Dose Rate, all particles, all flights including values on ground (Y)

(b) Total dose, all particles, all flights including values on ground (Y)

Figure 3.20: Average dose rate and total dose of all flights during the whole measurement time, which was different for each flight.

We can observe how the ground values (Y) in a 2-hour interval is almost 4 times lower than the lowest dose measured at flight altitudes. On the other hand, the dose given by the satellite in one hour at approximately 820 km altitude is more than 200 times higher than the highest dose measured in flight. It is also important to note how the total dose varies with respect to the dose rate depending on the exposure time. Although the Figure 3.20a shows that **B** flight is the one with the highest dose rate, as being a short flight, its total dose is not as significant as the dose of flight **F** for example (see Fig. 3.20b).

### 3.8 Linear-energy-transfer spectra

The Linear Energy Transfer (LET) is given by the ratio of the particle deposited energy ( $E$ ) along its trajectory to the cluster path length ( $L$ ) [22].

$$LET = \frac{E}{L} \quad (3.1)$$

The energy loss and particle LET were determined in the sensor material which in this case is Silicon. According to their stopping power, particles can be grouped into low LET events (muons, energetic electrons and X-rays) and high LET events (protons and heavy charged particles, also, e.g. fragmentation nuclear reactions with nuclei in the sensor volume). The event distributions, so called LET spectra for all particles is shown in Figure 3.21.

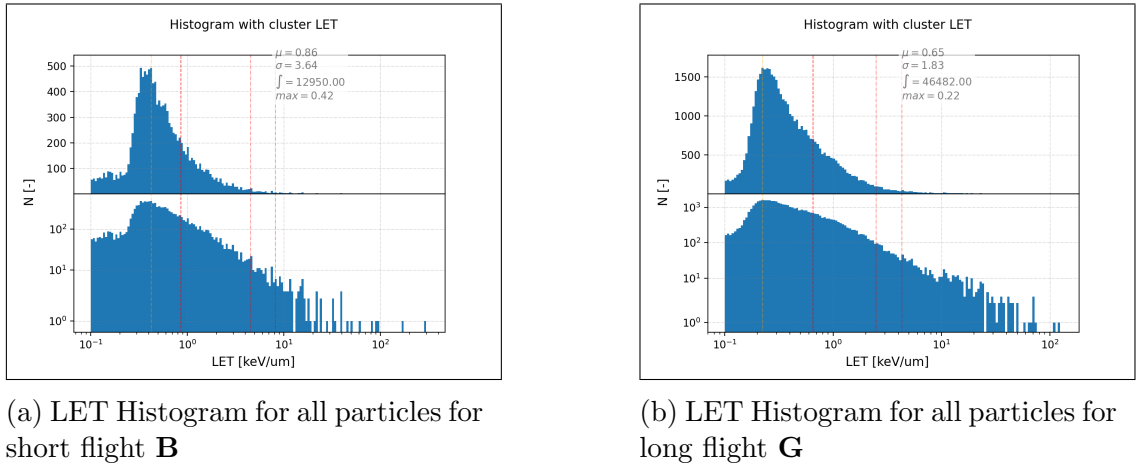


Figure 3.21: Linear energy transfer distributions

The results show that most particles exhibit low-LET power, which is below about 1 (keV/ $\mu\text{m}$ ), range that corresponds to LCPs (electrons, X and  $\gamma$  rays).

# Chapter 4

## Conclusions

The study and measuring of radiation fields at flight altitudes is important due to the potential health and safety risks for aircrew and passengers, effects of radiation on electronic components, space weather and avionics.

In this work, a total of 10 operational flight altitude data, measured in the aircraft passenger section, were used. Precise characterization, quantum sensitivity in terms of deposited energy and visualization of the charged particle radiation and X-ray field was performed by the semiconductor pixel detector Timepix operated in a miniaturized radiation camera MiniPIX-Timepix. Data processing was performed with an integrated SW tool (Data Processing Engine-DPE) provided by Advacam.

From the processed data, information including particle flux, deposited energy, dose rate and the equivalent deposited dose in the sampling time, field compo-



sition into broad particle classes (protons, electrons, X rays) as well as detailed visualization of the radiation field and quantum imaging registration of single particle tracks were obtained. To produce the graphs shown in Sec. 3, both python scripts provided by C. Granja as well as original python scripts were used.

Based on particle flux, particle classification and event count rates, the observed incidence of events showed a sudden increase just after takeoff, probably due to the aircraft ascending. On the other hand, the decrease in particle count, in the final seconds of the flight, coincides with the descent to ground. For measurement G, a clear increase in the detection of charged particles was observed for a period of approximately 2 hours before landing, which may indicate different flight altitudes or variations in the cosmic ray flux at long periods of flight.

In terms of deposited energy, the results confirmed that photons and electrons made up the majority of the particle counts. Energy distribution graphs for various particle types corroborate this result by showing that although protons and ions showed some sporadic energy peaks, they had a lower average energy deposition compared to photons and electrons. It is important to consider that, despite its scarce presence, the cumulative deposited energy of protons and ions emerged as a significant contributor to the total deposited energy.

The dose outcomes showed higher doses in the time interval after takeoff and before landing. Small variations toward the end of flight G were also evident in the corresponding analysis. We compared the in-flight measurements with those taken

on the ground (i.e. C. Granja and S. Pospisil, 2014 [5]) and by Prova satellite (i.e. C. Granja et al., 2016 [21]), from which it became evident that the dose rates during flight altitudes are substantially higher than the corresponding ground values. Furthermore, the satellite's dose rate, measured at an altitude of approximately 820 km, is considerably greater than the maximum dose rate detected during flight.

It should be noted that the total dose fluctuates as a function of exposure time relative to the dose rate. As an example of this, we can see that, although flight B presented the highest dose rate among all measurements, having a relatively short flight duration, it results in a less significant accumulated dose compared to flights such as F or E, which despite having a lower dose rate, accumulate a substantial total dose due to their long duration.

During this work, two principal measurements were analyzed in detail; results of the rest of the flights are presented in the annexes (Sec. 5).

As future work, an analysis with directional fluxes using the directional information from the detector as well as a future research article at a scientific journal will be considered.

# Chapter 5

## Annexes

### 5.1 Particle fluxes for remaining measurements

#### 5.1.1 Total particle flux, all particles

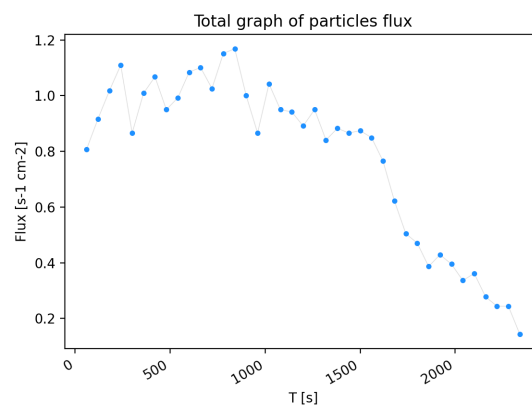


Figure 5.1: Total particle flux for the whole measurement **A**

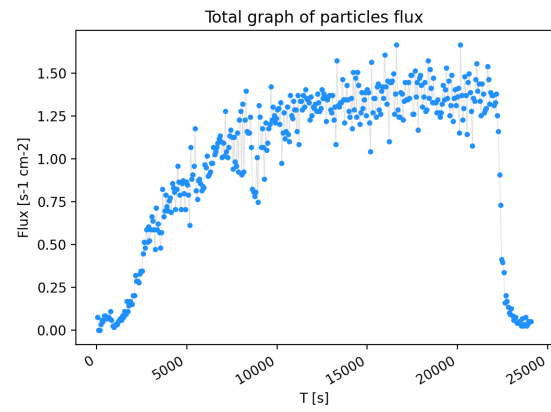


Figure 5.2: Total particle flux for the whole measurement **C**

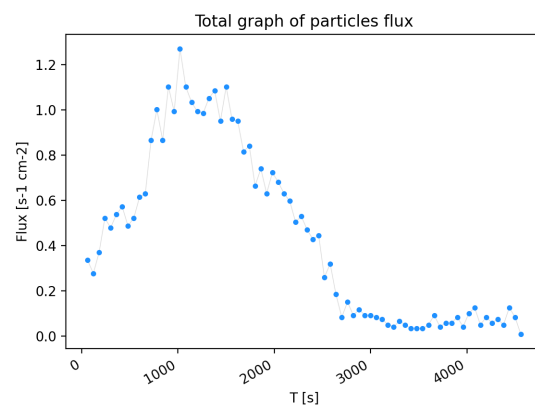


Figure 5.3: Total particle flux for the whole measurement **D**

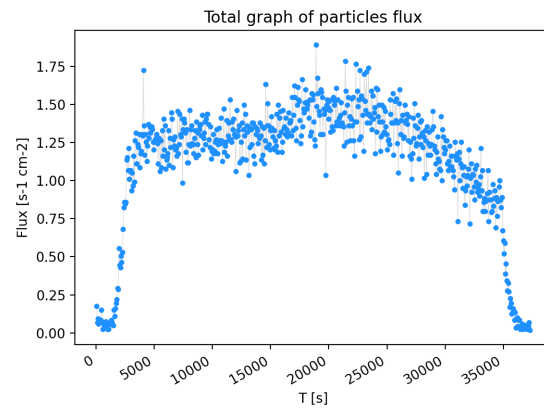


Figure 5.4: Total particle flux for the whole measurement **E**

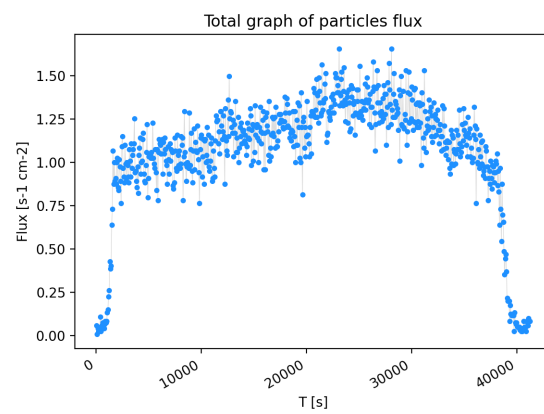


Figure 5.5: Total particle flux for the whole measurement **F**

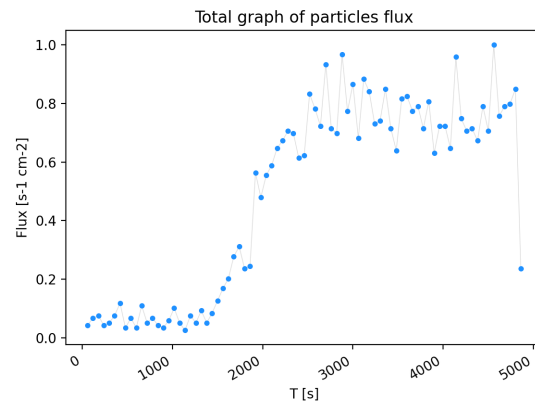


Figure 5.6: Total particle flux for the whole measurement **H**

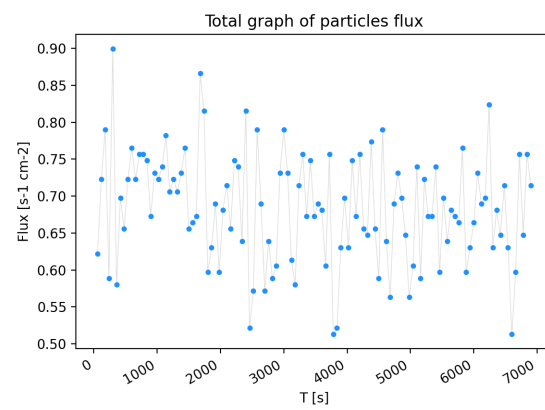


Figure 5.7: Total particle flux for the whole measurement **I**

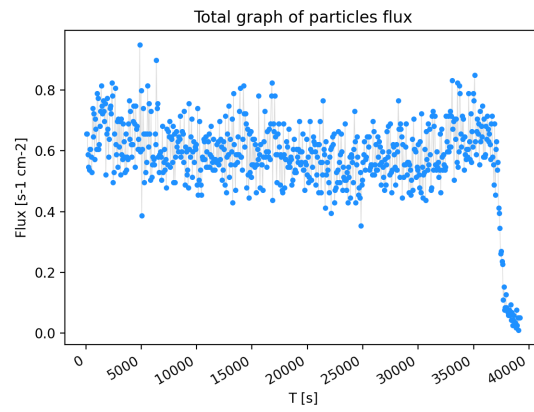


Figure 5.8: Total particle flux for the whole measurement **J**

### 5.1.2 Particle flux, according to particle class

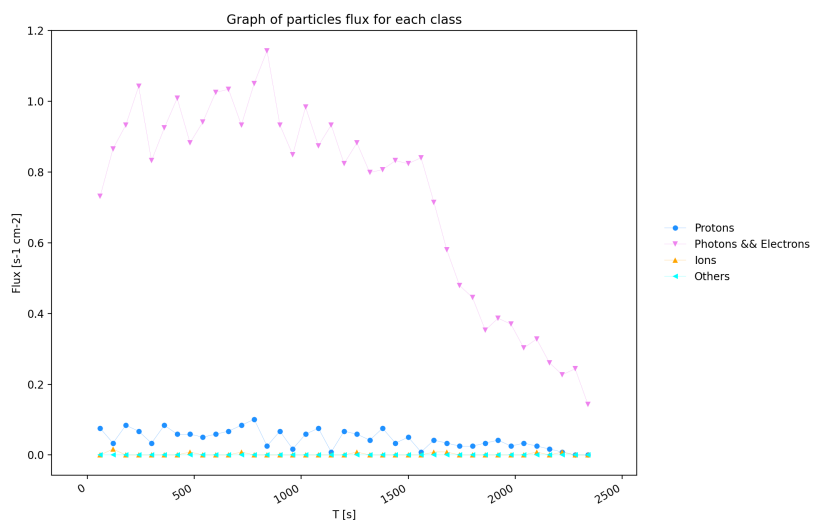
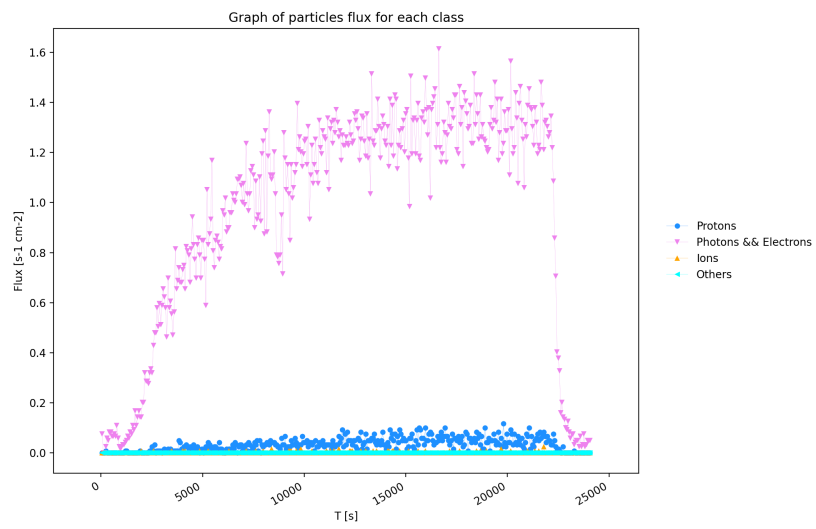
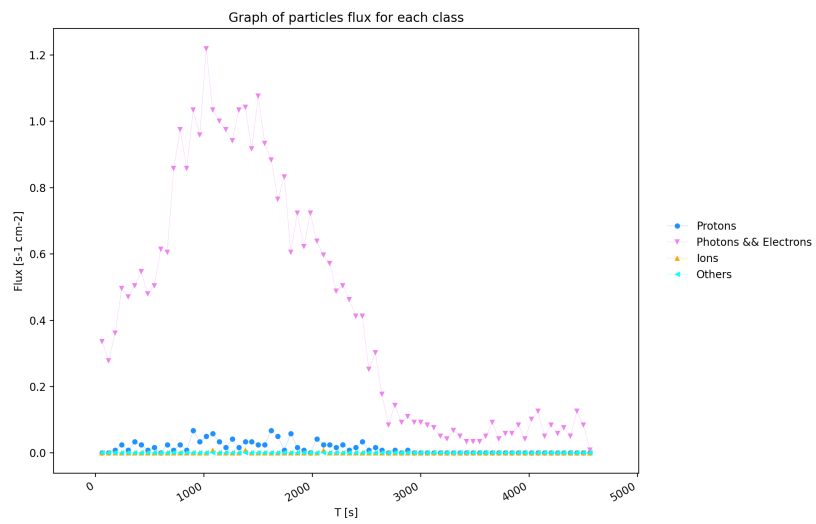
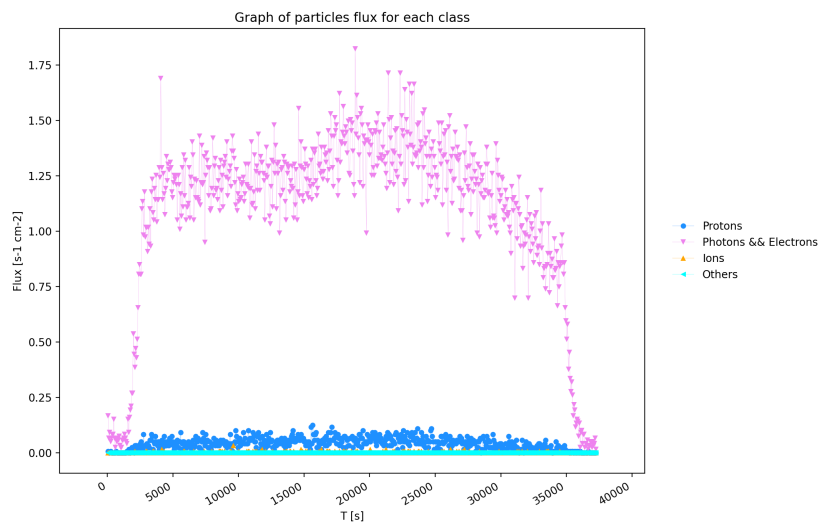
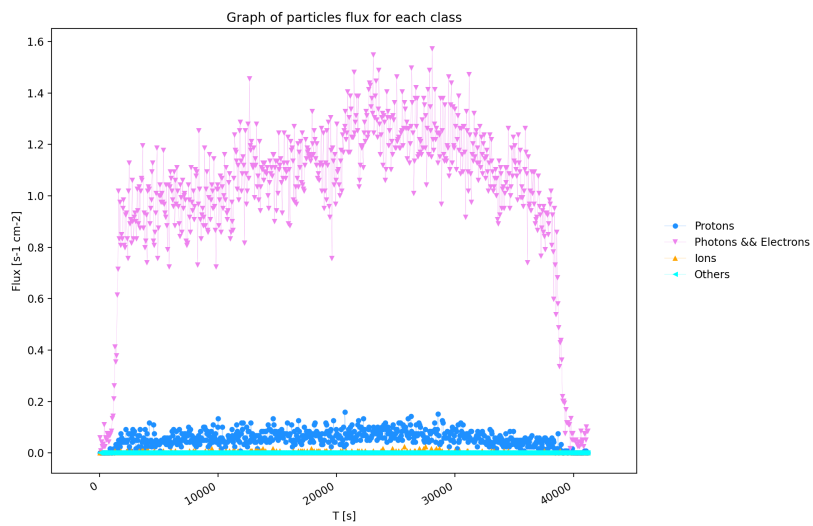
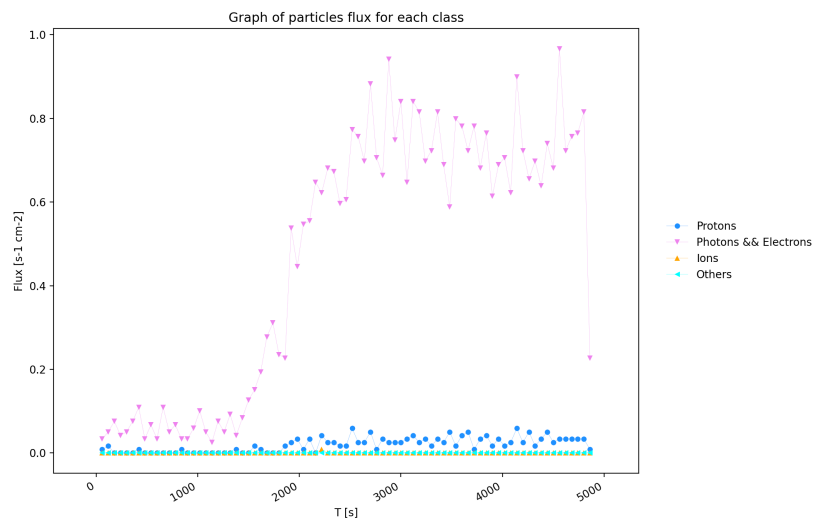
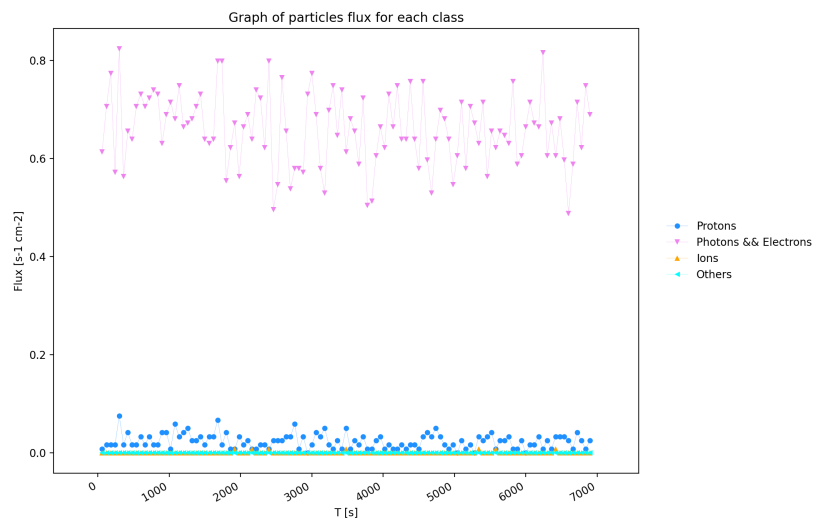


Figure 5.9: Particle flux for the whole measurement **A**



Figure 5.10: Particle flux for the whole measurement **C**Figure 5.11: Particle flux for the whole measurement **D**

Figure 5.12: Particle flux for the whole measurement **E**Figure 5.13: Particle flux for the whole measurement **F**

Figure 5.14: Particle flux for the whole measurement **H**Figure 5.15: Particle flux for the whole measurement **I**

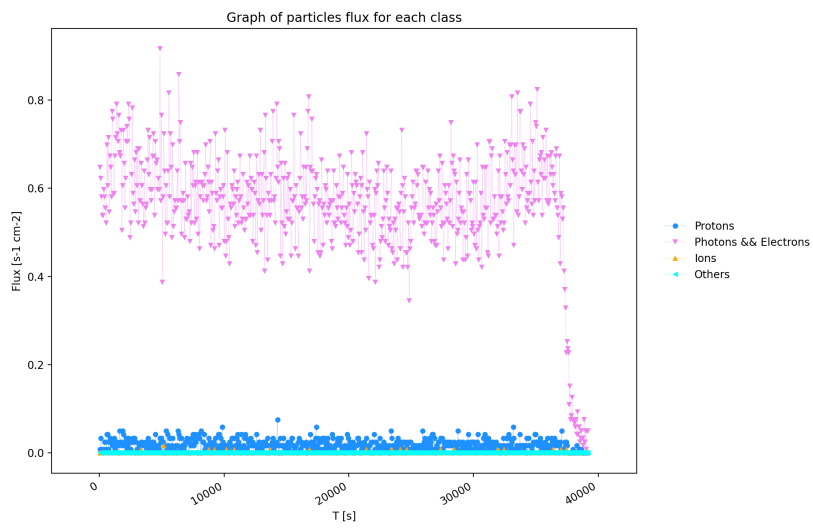


Figure 5.16: Particle flux for the whole measurement **J**

## 5.2 Deposited energy for remaining measurements

### 5.2.1 Deposited energy, all particles

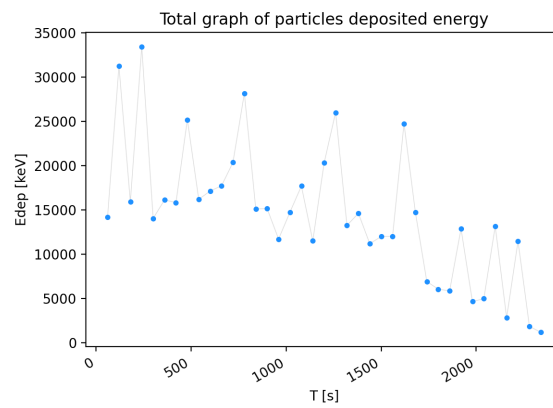


Figure 5.17: Deposited energy for the whole measurement **A**

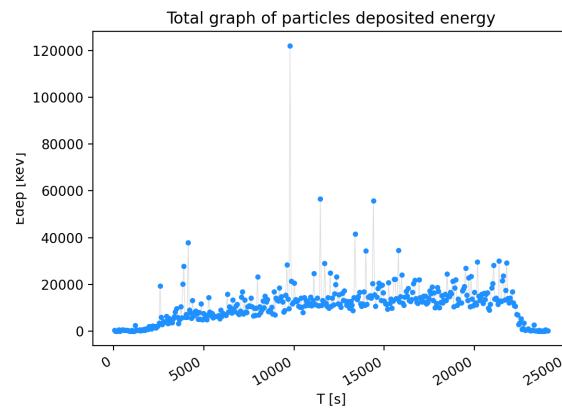


Figure 5.18: Deposited energy for the whole measurement **C**

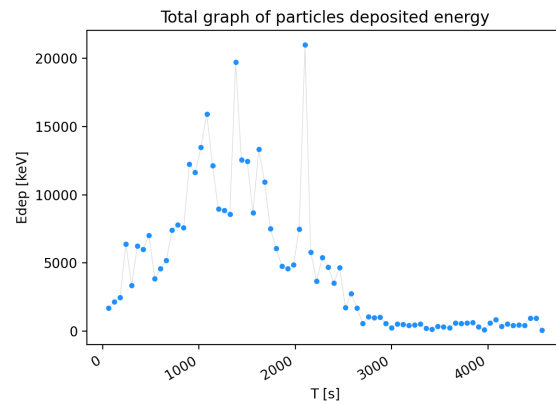


Figure 5.19: Deposited energy for the whole measurement **D**

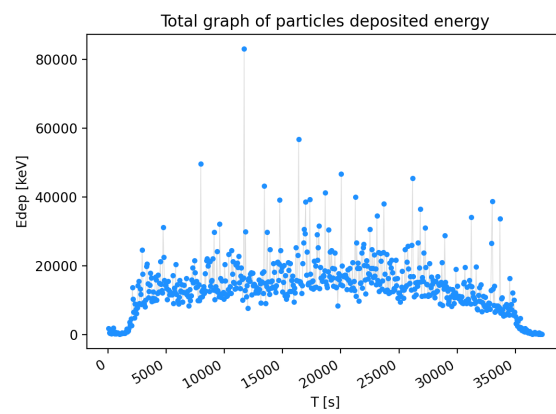


Figure 5.20: Deposited energy for the whole measurement **E**

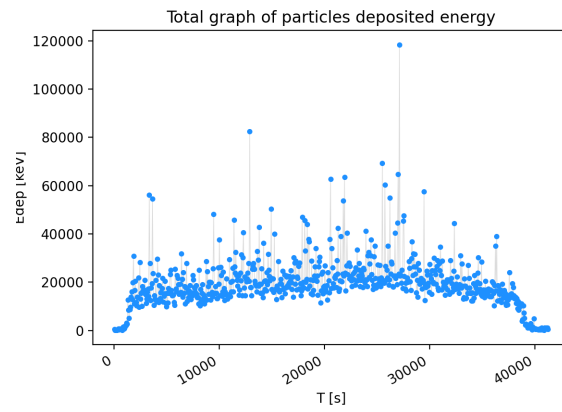


Figure 5.21: Deposited energy for the whole measurement **F**

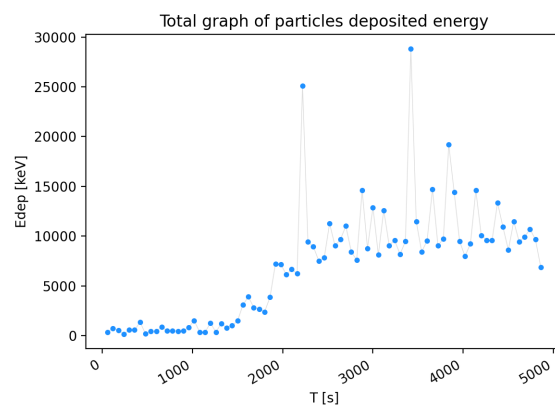


Figure 5.22: Deposited energy for the whole measurement **H**

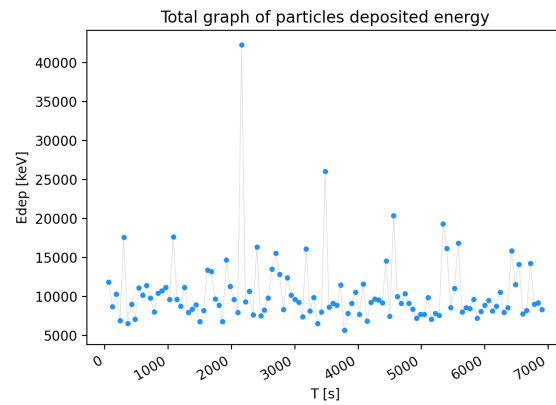


Figure 5.23: Deposited energy for the whole measurement **I**

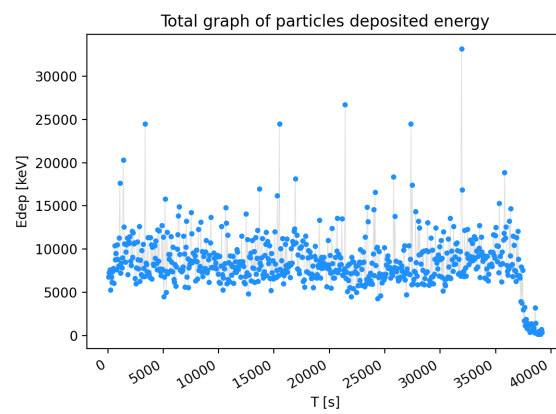


Figure 5.24: Deposited energy for the whole measurement **J**



## 5.2.2 Deposited energy according to particle class

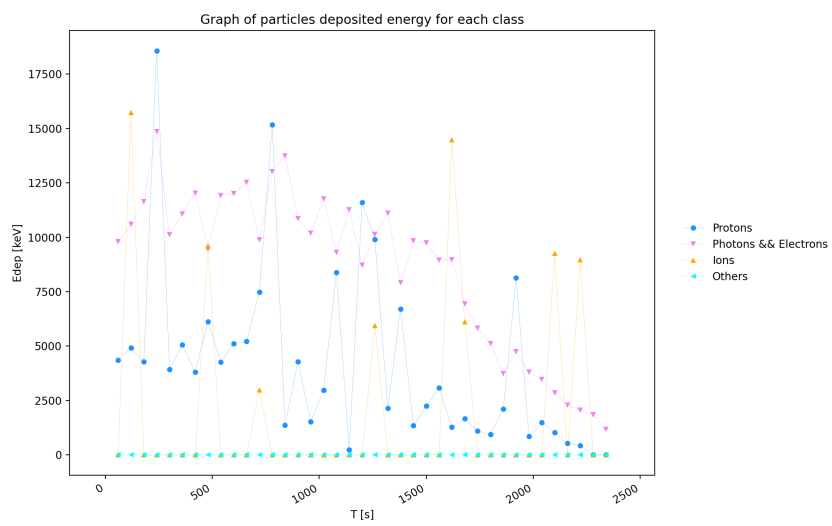


Figure 5.25: Deposited energy for the whole measurement **A**

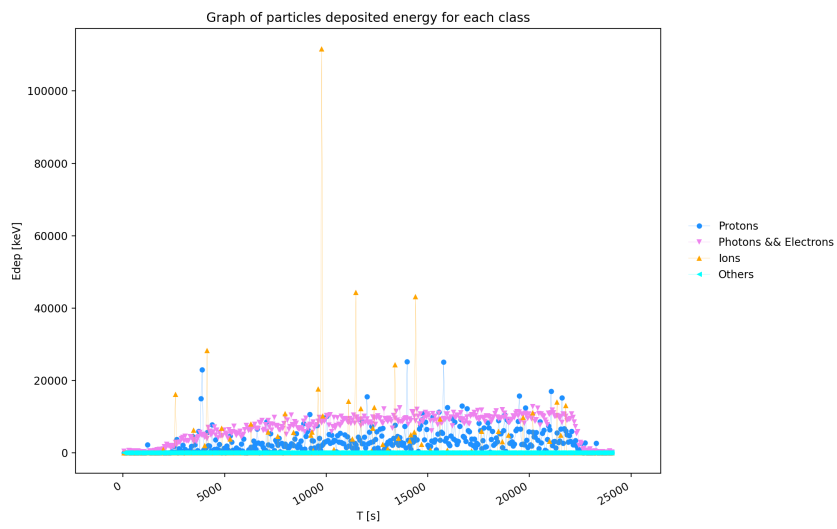


Figure 5.26: Deposited energy for the whole measurement **C**

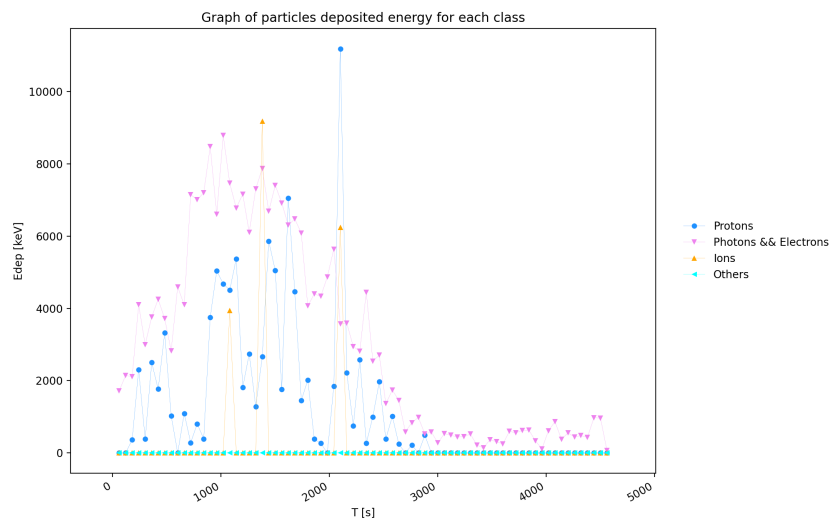
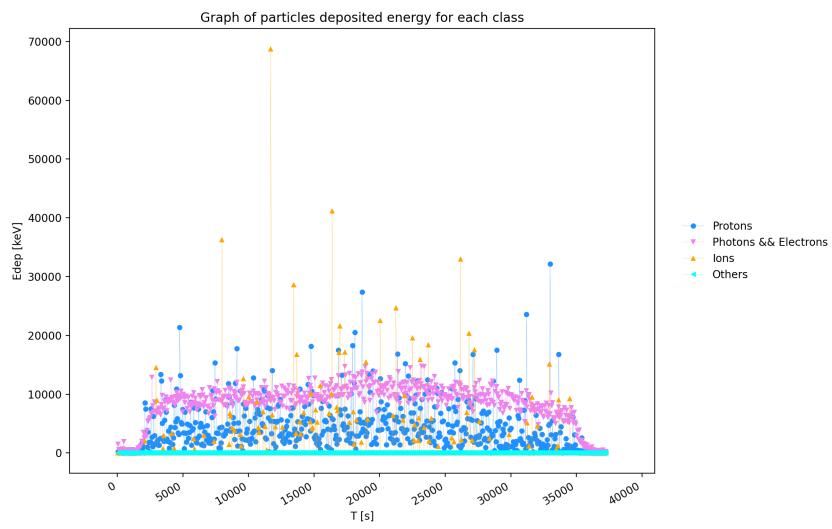
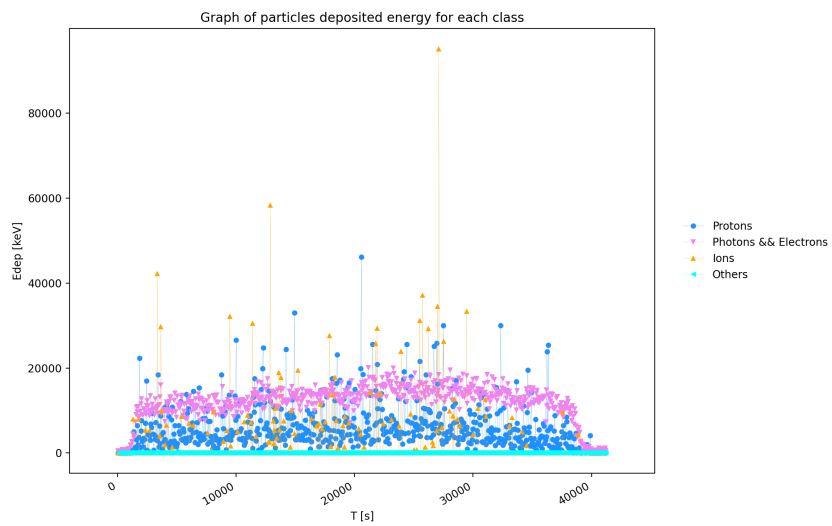


Figure 5.27: Deposited energy for the whole measurement **D**

Figure 5.28: Deposited energy for the whole measurement **E**Figure 5.29: Deposited energy for the whole measurement **F**

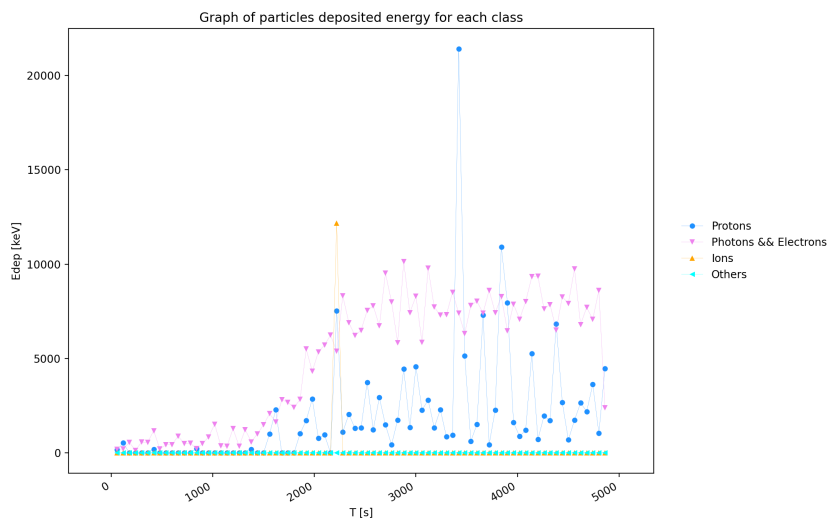


Figure 5.30: Deposited energy for the whole measurement **H**

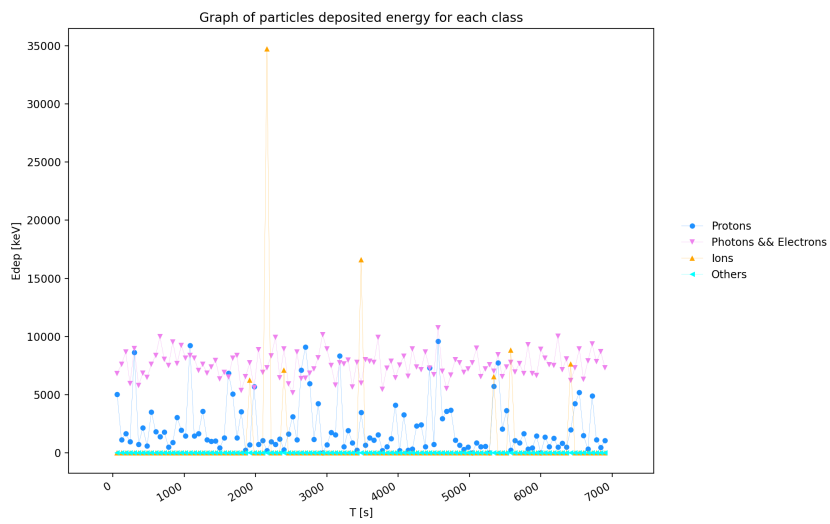


Figure 5.31: Deposited energy for the whole measurement **I**

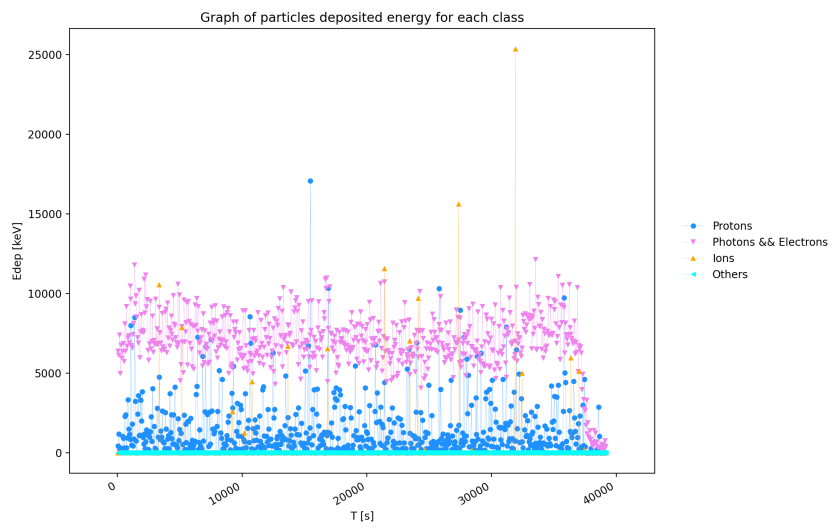


Figure 5.32: Deposited energy for the whole measurement **J**

## 5.3 Dose rate for remaining measurements

### 5.3.1 Total dose rate, all particles

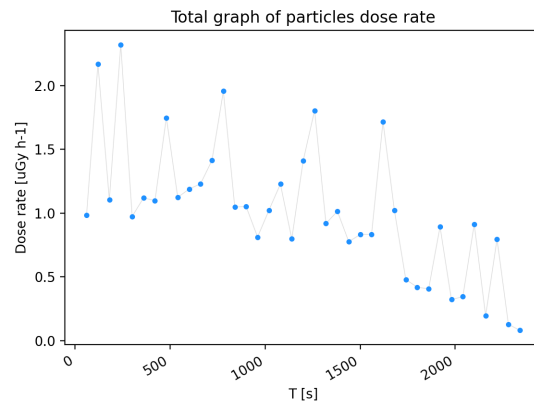


Figure 5.33: Dose rate for the whole measurement **A**

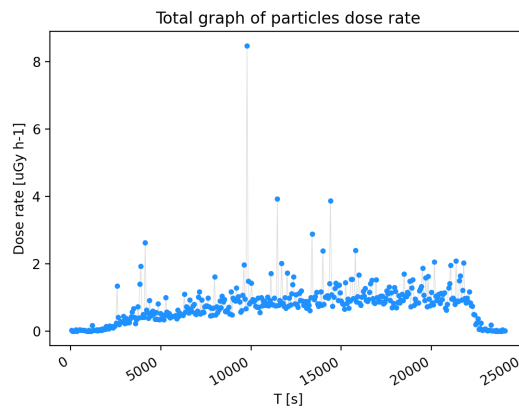
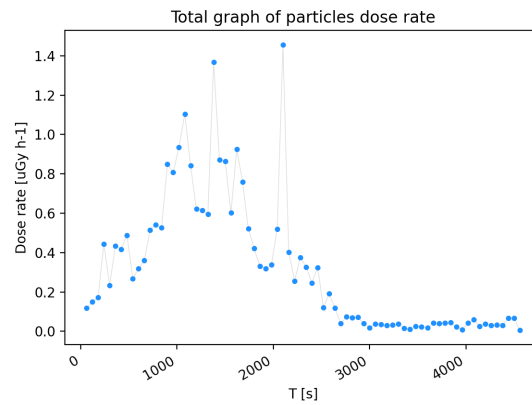
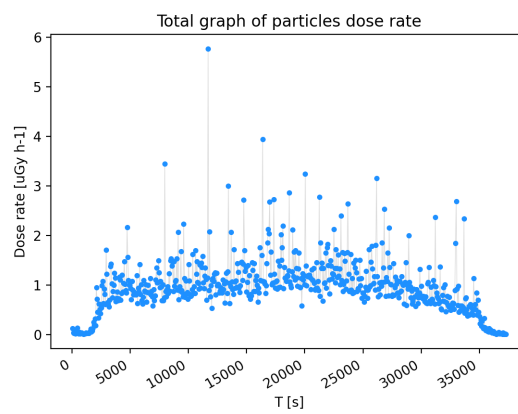
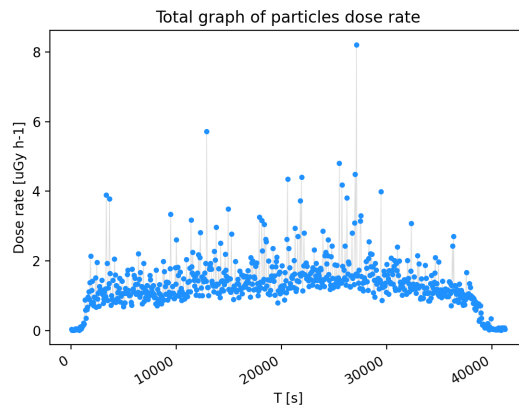
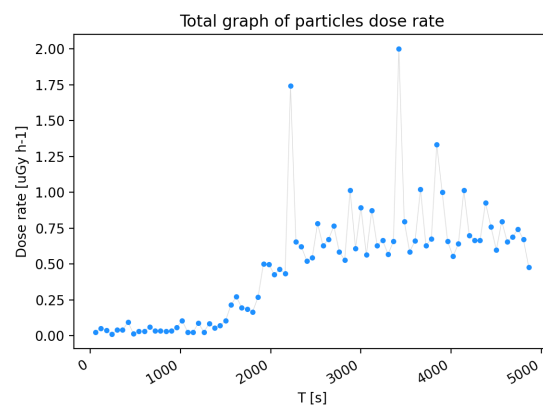
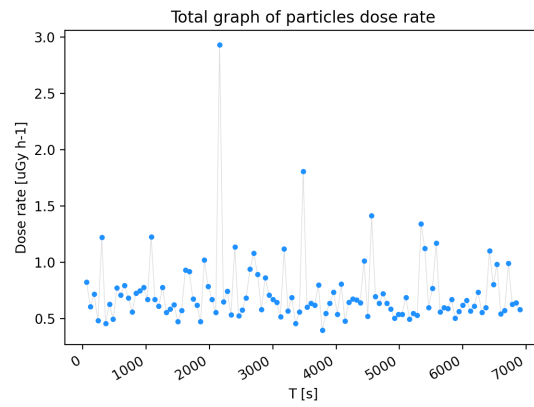
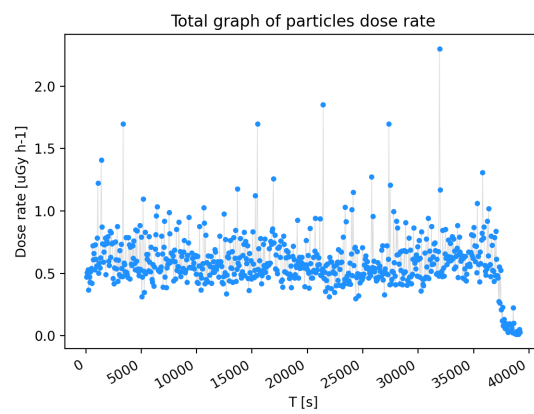


Figure 5.34: Dose rate for the whole measurement **C**

Figure 5.35: Dose rate for the whole measurement **D**Figure 5.36: Dose rate for the whole measurement **E**

Figure 5.37: Dose rate for the whole measurement **F**Figure 5.38: Dose rate for the whole measurement **H**



Figure 5.39: Dose rate for the whole measurement **I**Figure 5.40: Dose rate for the whole measurement **J**

### 5.3.2 Dose rate according to particle class

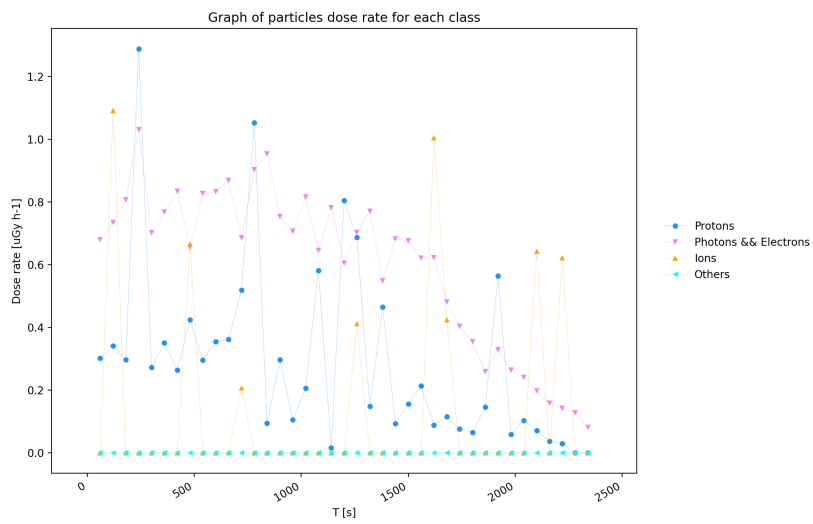
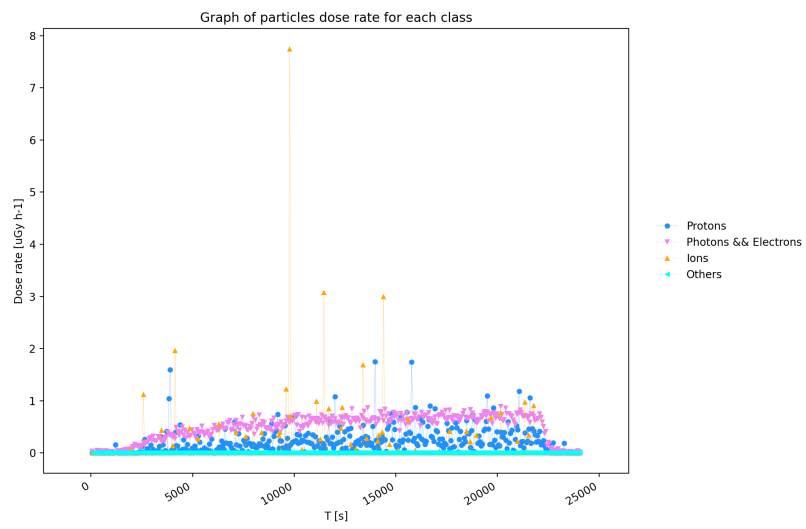
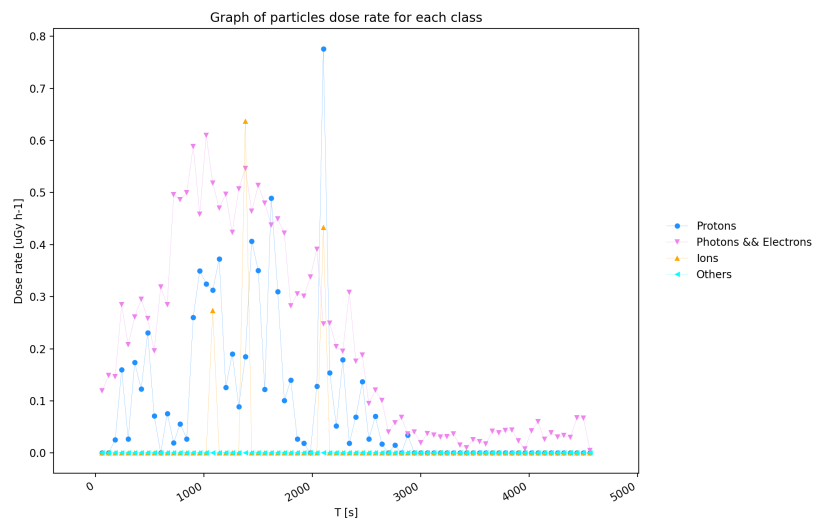
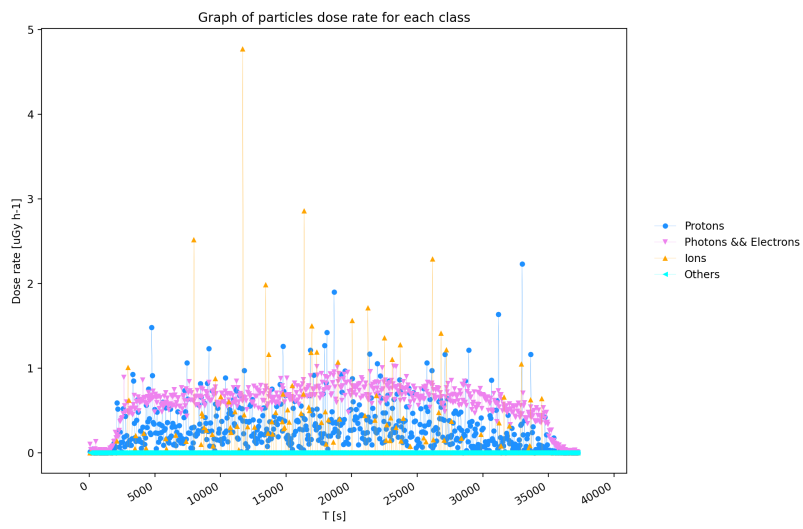
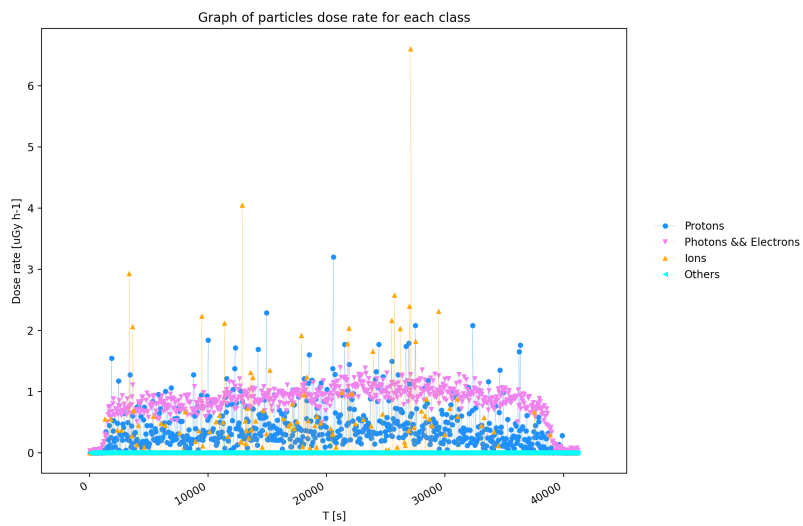
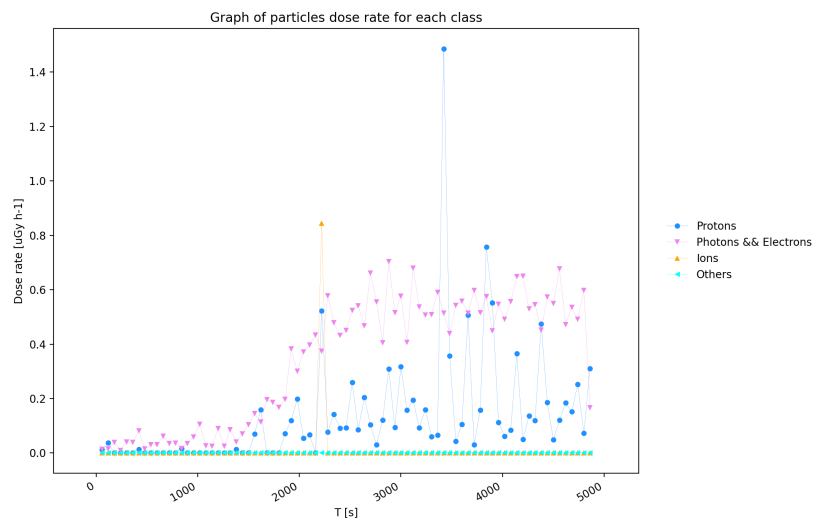
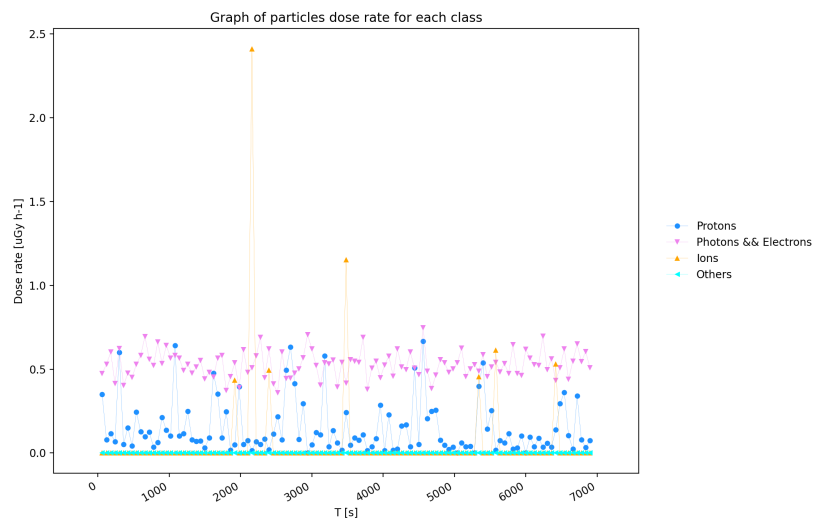


Figure 5.41: Dose rate for the whole measurement **A**

Figure 5.42: Dose rate for the whole measurement **C**Figure 5.43: Dose rate for the whole measurement **D**

Figure 5.44: Dose rate for the whole measurement **E**Figure 5.45: Dose rate for the whole measurement **F**

Figure 5.46: Dose rate for the whole measurement **H**Figure 5.47: Dose rate for the whole measurement **I**

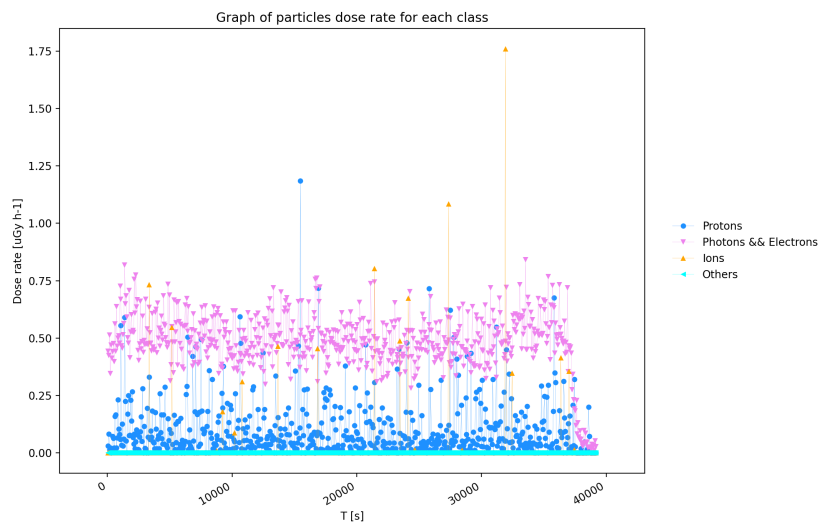


Figure 5.48: Dose rate for the whole measurement **J**

# Bibliography

- [1] F. Spurny; O. Ploc; I. Jadrníčková; K. Turek; T. Dachev; M. Gelev. Monitoring of onboard aircraft exposure to cosmic radiation: May–december 2005. *Advances in Space Research*, pages 1551–1556, 2007.
- [2] R. Beaujean; S. Burmeister; F. Petersen and G. Reitz. Radiation exposure measurement onboard civil aircraft. *Example*, page 312–315, 2005.
- [3] Oxford: Pergamon Press. International commission on radiological protection. 1990 recommendations of the international commission on radiological protection. *ICRP Publication 60. Ann. ICRP*, page 21(1–3), 1991.
- [4] Jones; J.B.L.; Bentley; R. Hunter; et al. Space weather and commercial airlines. pages 36, 2258–2267, 2005.
- [5] C. Granja and S. Pospisil. Quantum dosimetry and online visualization of x-ray and charged particle radiation in commercial aircraft at operational flight altitudes with the pixel detector timepix. *Advances in Space Research*, pages 241–251, 2014.

- [6] F.H.Attix. Introduction to radiological physics and radiation dosimetry. pages 2–3, 1986.
- [7] Glenn E Knoll. *Radiation Detectibn and Measurement*. John Wiley Sons, Inc., 2000.
- [8] C. Granja; et al. Minipix timepix3 — a miniaturized radiation camera with onboard data processing for online characterization of wide-intensity mixed-radiation fields. *International Workshop on Radiation Imaging Detectors*, 2021.
- [9] Icru. international commision on radiation units and measurements. *Radiation quantities and units. Report 19*, 1971.
- [10] Otto Claus Allkofer and Peter Karl Grieder. Cosmic rays on earth. 1984.
- [11] R. Beaujean; S. Burmeister; F. Petersen and G. Reitz. Radiation exposure measurement onboard civil aircraft. *Radiation Protection Dosimetry*, 2005.
- [12] A.Alikhanyan. Cosmic ray division. national laboratory.
- [13] C. Granja; C. Oancea; J. Jakubek; et al. Wide-range tracking and let-spectra of energetic light and heavy charged particles. *Nuclear Inst. and Methods in Physics Research*, 20021.
- [14] C. Granja; K. Kudela; J. Jakubek; P. Krist; et al;. Directional detection of charged particles and cosmic rays with the miniaturized radiation camera minipix timepix. *Nuclear Inst. and Methods in Physics Research, A*, pages 142–152, 2018.



- [15] C. Granja; J. Jakubek; S. Polansky; V. Zach; et al;. Resolving power of pixel detector timepix for wide-range electron, proton and ion detection. *Nuclear Inst. and Methods in Physics Research, A*, pages 60–71, 2018.
- [16] ADVACAM. <https://advacam.com/camera/minipix>. Minipix datasheet.
- [17] <https://advacam.com/minipix>.
- [18] C. Granja; J. Jakubek; et al. Spectral and directional sensitive composition characterization of mixed radiation fields with the miniaturized radiation camera minipix timepix2. *Journal of Instrumentation*, 2022.
- [19] ADVACAM. <https://wiki.advacam.cz/index.php/DPE>. Dpe.
- [20] J.W. Poston. Encyclopedia of physical science and technology (third edition). *Example*, pages 603–650, 2003.
- [21] C. Granja and S. Polansky. The satram timepix spacecraft payload in open space on board the proba-v satellite for wide range radiation monitoring in leo orbit. 2016.
- [22] C. Granja; C. Oancea; J. Jakubek; et al. Wide-range tracking and let-spectra of energetic light and heavy charged particles. *Nucl. Instrum. and Methods A* 988, 2021.